

Instability of microbial droplets growing on viscous substrates

Vicente Gomez Herrera^{1,2} and Scott Weady²

¹Courant Institute of Mathematical Sciences, New York University, New York, NY 10012, USA

²Center for Computational Biology, Flatiron Institute, New York, NY 10010, USA

Corresponding author: Scott Weady, sweady@flatironinstitute.org

(Received xx; revised xx; accepted xx)

We develop and analyze a model for a flat microbial droplet growing on the surface of a three-dimensional viscous fluid. The model describes growth-induced stresses at the fluid surface, density variations in the bulk due to nutrient consumption, and the resulting fluid flows that arise. We reformulate this free-boundary problem as a system of integro-differential equations defined solely on the microbial domain. From this formulation, we identify an axisymmetric solution corresponding to a radially expanding disk and analyze its morphological stability. We find that growth forces stabilize the axisymmetric solution while buoyancy forces destabilize it. We connect these findings to experimental observations.

1. Introduction

Microbial communities are strongly influenced by the environments they inhabit. For example, the growth and morphology of bacterial colonies and biofilms depends on substrate composition and rheology (Fei *et al.* 2020; Asp *et al.* 2022; Faiza *et al.* 2025; Gonzalez La Corte *et al.* 2025), substrate topography controls motility and nutrient accessibility (Chang *et al.* 2015; Gu *et al.* 2016; Postek *et al.* 2024), and ambient fluid flows affect morphology and population dynamics (Perlekar *et al.* 2010; Pearce *et al.* 2019; Benzi *et al.* 2022). These features, in many cases, arise from a feedback loop between growth, mechanics, and chemical sensing (Hallatschek *et al.* 2023).

Microbial communities at or near fluid interfaces arise in a variety of culinary, industrial, and environmental contexts and present a particularly interesting case (Vaccari *et al.* 2017). Examples include kilometer-scale algal blooms that are mixed by turbulent oceanic flows (Abraham 1998; Hallegraeff 2003), centimeter-scale pellicles that facilitate kombucha fermentation (Aung & Kim 2024), and millimetric biofilms on oil droplets that can aid in bioremediation (Vaccari *et al.* 2015; Hickl & Juarez 2022; Prasad *et al.* 2023). Experiments of yeast colonies (*S. cerevisiae*) growing on viscous substrates found that metabolically generated flows, which arise from depletion of dense nutrients in the bulk, can enhance nutrient transport and drive interfacial instabilities (Atis *et al.* 2019; Narayanasamy *et al.* 2025). Particle image velocimetry measurements and simulations of a hydrodynamic model

show these metabolic flows manifest as a vortex ring in the bulk and a local maximum in the surface velocity outside of the colony. It remains, however, unclear how these flows, along with those generated by growth, connect to the colony morphology.

This type of system – a microbial “droplet” growing on the surface of a viscous fluid – belongs to a more general class of problems involving immiscible materials suspended on a fluid interface. Such systems can be found in many contexts, with examples including surfactants (Stone & Leal 1990; Lubensky & Goldstein 1996; Alexander *et al.* 2007; Manikantan & Squires 2020; Jia & Shelley 2022), ice sheets (Chakrabarti 2000; Williams & Squire 2004; Askham *et al.* 2025), lipid membranes (Saffman & Delbrück 1975; Saffman 1976; Stone & McConnell 1995; Stone & Ajdari 1998), and thin layers of active particles (Masoud & Shelley 2014; Fei *et al.* 2017; Jia *et al.* 2022). Models within this class often involve a partial differential equation (PDE) for the bulk fluid velocity, such as the Stokes equations or potential flow, coupled to a constitutive law for the internal mechanics of the droplet. This results in a challenging boundary value problem with complex boundary conditions. One effective approach is to reformulate the coupled surface-bulk problem as an integro-differential equation defined solely over the droplet. This significantly reduces the degrees of freedom, though the integral operators are typically singular and must be treated with care.

In this work, we develop and analyze a mathematical model for a microbial droplet growing, through consumption of an underlying nutrient, on the surface of a viscous fluid. The model takes the form of a free-boundary problem driven by three coupled components: (1) An isotropic pressure internal to the evolving droplet arising from growth, (2) bulk fluid flow driven by this growth pressure, and (3) buoyancy-driven flows arising from consumption of a nutrient. In section 2 we present the partial differential equations governing the full three-dimensional system. Dimensional analysis and asymptotic reduction simplifies these nonlinear equations to a set of linear PDEs. In section 3 we exploit this linearity to reformulate the model as a system of integro-differential equations defined solely on the droplet. In this formulation, several integral operators appear whose spectral properties we discuss in section 4. These properties provide a clear route to axisymmetric solutions, which we derive in section 5. Finally, in section 6 we analyze the geometric stability of these axisymmetric solutions. This analysis shows growth stabilizes axisymmetric geometries while flows induced by nutrient consumption amplify perturbations. These results offer a rigorous mechanical explanation of the morphological instabilities observed in experiments of growing yeast colonies (Atis *et al.* 2019), and provide a robust mathematical framework for the analysis of microbial communities growing on fluid interfaces.

2. A mathematical model

We consider a two-dimensional microbial droplet $\Omega(t) \subset S$ growing on the surface $S = \partial V = \{X = (x, y, 0) \in \mathbb{R}^3\}$ of a semi-infinite volume $V = \{X = (x, y, z) \in \mathbb{R}^3 : z < 0\}$ of a Newtonian fluid. A schematic of this configuration is shown in Fig. 1. As the droplet expands, it exerts forces at the fluid surface which drive bulk flows. Simultaneously, microbial nutrient consumption establishes density gradients in the underlying fluid volume which lead to buoyancy-induced flows. The variables to be determined are therefore the bulk fluid velocity $\mathbf{U} : V \rightarrow \mathbb{R}^3$ and pressure $P : V \rightarrow \mathbb{R}$, the nutrient concentration $c : V \rightarrow \mathbb{R}$ and fluid density $\rho(c) : V \rightarrow \mathbb{R}$, and the surface growth velocity $\mathbf{u} : \Omega \rightarrow \mathbb{R}^2$ and growth pressure $p : \Omega \rightarrow \mathbb{R}$, which will be related through constitutive laws and boundary conditions. In the following we will need to restrict quantities in the fluid volume to the fluid surface. This is conveniently described by the operator

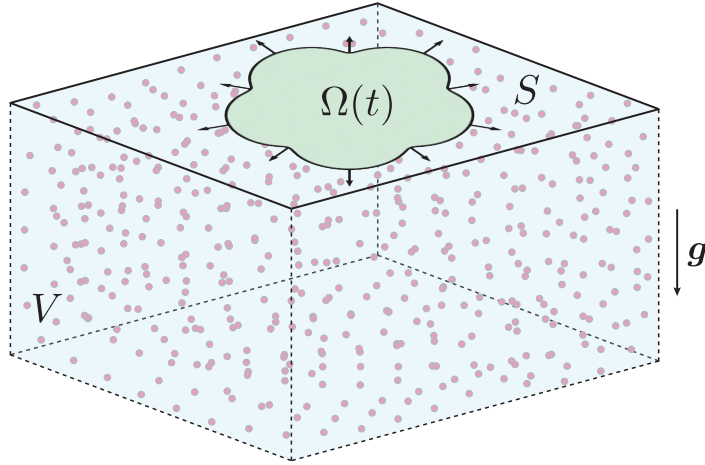


Figure 1. Schematic of the mathematical model. A growing microbial droplet $\Omega(t)$ (green) sits on the surface S of a semi-infinite fluid volume V (blue). As the droplet grows, it depletes dense nutrients (red circles) in the fluid which drives buoyant flows.

T which takes a vector field over V to its tangential component on the surface, e.g. $T[(U_x(x, y, z), U_y(x, y, z), U_z(x, y, z))] (x, y) = (U_x(x, y, 0), U_y(x, y, 0))$.

2.1. Fluid

We assume the substrate is a Newtonian fluid with constant viscosity μ and variable density ρ . Conservation of momentum and mass in the fluid are

$$\rho \left(\frac{\partial \mathbf{U}}{\partial t} + \mathbf{U} \cdot \nabla_{3D} \mathbf{U} \right) = -\nabla_{3D} P + \mu \Delta_{3D} \mathbf{U} - \rho g \mathbf{e}_z \quad \text{in } V, \quad (2.1)$$

$$\frac{\partial \rho}{\partial t} + \nabla_{3D} \cdot (\rho \mathbf{U}) = 0 \quad \text{in } V, \quad (2.2)$$

where g is acceleration due to gravity. Here $\nabla_{3D} = (\partial_x, \partial_y, \partial_z)$ is the three-dimensional gradient and $\Delta_{3D} = \partial_x^2 + \partial_y^2 + \partial_z^2$ is the three-dimensional Laplacian, with an analogous definition for ∇_{2D} and Δ_{2D} .

The nutrient field c within the fluid satisfies the advection-diffusion equation

$$\frac{\partial c}{\partial t} + \nabla_{3D} \cdot (c \mathbf{U}) = D \Delta_{3D} c \quad \text{in } V, \quad (2.3)$$

where D is a diffusion constant. For simplicity, we assume the density increases linearly with the nutrient field, $\rho(c) = \rho_0(1 + \alpha c)$, where ρ_0 is the fluid density in the absence of nutrients and $\alpha > 0$ is a constant. Making the Boussinesq approximation, Eqs. (2.1)-(2.2) become

$$\rho_0 \left(\frac{\partial \mathbf{U}}{\partial t} + \mathbf{U} \cdot \nabla_{3D} \mathbf{U} \right) = -\nabla_{3D} P + \mu \Delta_{3D} \mathbf{U} - \rho_0 \alpha c g \mathbf{e}_z \quad \text{in } V, \quad (2.4)$$

$$\nabla_{3D} \cdot \mathbf{U} = 0 \quad \text{in } V, \quad (2.5)$$

where we've absorbed the hydrostatic pressure: $P \mapsto P - \rho_0 g z$.

2.2. Growth

Defining $\gamma(c)$ to be the microbial areal growth rate, the two-dimensional divergence of the surface velocity satisfies

$$\nabla_{2D} \cdot \mathbf{u} = \gamma(c) \quad \text{in } \Omega. \quad (2.6)$$

The functional form of γ is a modeling choice but should be restricted by physical considerations. In particular, we expect γ to be non-negative, non-decreasing, bounded, and satisfy $\gamma(0) = 0$.

2.3. Boundary conditions

On the droplet, growth forces are balanced by viscous forces. Letting $\mathbf{f} = [-P\mathbf{I}_{3D} + \mu(\nabla_{3D}\mathbf{U} + \nabla_{3D}\mathbf{U}^T)] \cdot \mathbf{e}_z$ be the traction vector at the surface, we have

$$\begin{cases} T[\mathbf{f}] = -\nabla_{2D}p & \text{on } \Omega, \\ T[\mathbf{U}] = \mathbf{u} & \text{on } \Omega, \\ \mathbf{U} \cdot \mathbf{e}_z = 0 & \text{on } \Omega. \end{cases} \quad (2.7)$$

The first condition describes the tangential force balance associated with the growth pressure p , the second is the no-slip condition, and the third requires that the surface remains flat. Further, we assume the pressure vanishes on the boundary of the droplet,

$$p = 0 \quad \text{on } \partial\Omega. \quad (2.8)$$

Note that the growth pressure is *not* the restriction of the three-dimensional fluid pressure P to S . Outside of the droplet we have

$$\begin{cases} T[\mathbf{f}] = \mathbf{0} & \text{on } S \setminus \Omega, \\ \mathbf{U} \cdot \mathbf{e}_z = 0 & \text{on } S \setminus \Omega, \end{cases} \quad (2.9)$$

with suitable boundary conditions at infinity.

Outside of the droplet, the concentration field satisfies the boundary conditions

$$\begin{cases} \frac{\partial c}{\partial z} = 0 & \text{on } S \setminus \Omega, \\ c \rightarrow c_\infty & \text{as } |X| \rightarrow \infty. \end{cases} \quad (2.10)$$

The first equation says there is no nutrient flux on the open surface while the second sets nutrient supply in the far-field. On the droplet, the boundary condition arises from conservation of mass. Specifically, letting $\rho_b(\mathbf{x})$ be the microbial mass per unit area, which has units of kg/m^2 , the flux of the total microbial mass $m_b = \int_{\Omega} \rho_b \, d\mathbf{x}$ is

$$\dot{m}_b = \int_{\Omega} \left(\frac{\partial \rho_b}{\partial t} + \nabla_{2D} \cdot (\mathbf{u} \rho_b) \right) \, d\mathbf{x}. \quad (2.11)$$

Similarly, the flux of the nutrient mass $m_c = \int_V c \, d\mathbf{X}$ is

$$\dot{m}_c = D \left(\int_{\Omega} \nabla c \cdot \hat{\mathbf{n}} \, d\mathbf{x} \right). \quad (2.12)$$

Enforcing $\dot{m}_b + \dot{m}_c = 0$, assuming ρ_b is constant, and using $\nabla_{2D} \cdot \mathbf{u} = \gamma(c)$, this yields the Robin-type boundary condition

$$D \frac{\partial c}{\partial z} = -\rho_b \gamma(c) \quad \text{on } \Omega. \quad (2.13)$$

Finally, owing to growth, Ω will evolve in time. Letting $\Gamma(\theta) : [0, 2\pi) \rightarrow \partial\Omega$ be a parameterization of the boundary of Ω , this evolution is given by the kinematic condition

$$\frac{\partial \Gamma}{\partial t} = (\mathbf{u}|_{\Gamma} \cdot \hat{\mathbf{n}}) \hat{\mathbf{n}}, \quad (2.14)$$

where $\hat{\mathbf{n}}$ is the outward normal vector to Ω , which is parallel to the surface S .

2.4. Dimensional analysis

The full set of equations is complex and nonlinear. However, through dimensional analysis and asymptotic approximations, we can reduce the system to a set of linear PDEs. Here we choose as a characteristic length scale $\ell_c = (|\Omega_0|/\pi)^{1/2}$ (e.g. the radius for an initially circular domain), time scale based on the characteristic growth rate $t_c = 1/\gamma_\infty$ with $\gamma_\infty = \gamma(c_\infty)$ the saturated growth rate, pressure scale μ/t_c , and concentration scale c_∞ . Denoting dimensionless variables by primes, equations (2.4)-(2.5) in dimensionless form are

$$Re \left(\frac{\partial \mathbf{U}'}{\partial t'} + \mathbf{U}' \cdot \nabla'_{3D} \mathbf{U}' \right) = -\nabla'_{3D} P' + \Delta'_{3D} \mathbf{U}' - Ra c' \mathbf{e}_z \quad \text{in } V', \quad (2.15)$$

$$\nabla'_{3D} \cdot \mathbf{U}' = 0 \quad \text{in } V', \quad (2.16)$$

where $Re = (\ell_c^2/t_c)/(\mu/\rho_0)$ is the Reynolds number, which compares the areal growth rate to momentum diffusion, and $Ra = (\rho_0 \alpha c_\infty g \ell_c^3)/(\mu \ell_c^2/t_c)$ is the metabolic Rayleigh number, which compares buoyancy forces to growth forces. Similarly, the concentration equation (2.3) becomes

$$Pe \left(\frac{\partial c'}{\partial t'} + \mathbf{U}' \cdot \nabla'_{3D} c' \right) = \Delta' c' \quad \text{in } V', \quad (2.17)$$

where $Pe = (\ell_c^2/t_c)/D$ is the Péclet number, which compares the areal growth rate to nutrient diffusion. The divergence condition on Ω becomes

$$\nabla'_{2D} \cdot \mathbf{u}' = \gamma'(c') \quad \text{on } \Omega', \quad (2.18)$$

and the corresponding flux condition is

$$\frac{\partial c'}{\partial z'} = -\beta \gamma'(c'), \quad (2.19)$$

where $\beta = (\rho_b \gamma_\infty \ell_c)/(c_\infty D)$. (Note that here $\gamma'(c') = \gamma(c_\infty c')/\gamma_\infty$.) Finally, the concentration satisfies $c' \rightarrow 1$ in the far-field. All other boundary conditions keep the same form.

Assuming $Re, Pe \ll 1$, the dimensionless velocity and pressure satisfy the forced Stokes equations

$$-\nabla'_{3D} P' + \Delta'_{3D} \mathbf{U}' - Ra c' \mathbf{e}_z = \mathbf{0} \quad \text{in } V', \quad (2.20)$$

$$\nabla'_{3D} \cdot \mathbf{U}' = 0 \quad \text{in } V', \quad (2.21)$$

and the dimensionless concentration satisfies the Laplace equation

$$\Delta'_{3D} c' = 0 \quad \text{in } V'. \quad (2.22)$$

This asymptotic limit is significantly more tractable mathematically as the PDEs are linear and elliptic in the fluid volume, with all nonlinearity and time dependence coming from boundary conditions and geometry.

From a physical standpoint, the limit $Re, Pe \ll 1$ holds when $\gamma_\infty |\mathcal{Q}_0| \ll \mu/\rho_0, D$, which occurs for small microbial droplets with slow growth. We can estimate these parameters for the experiments of Atis *et al.* (2019) with the characteristic colony size $\ell_c = R \approx 2.5$ mm, time scale $t_c = 1/\gamma_\infty \approx 1$ day, viscosity $\mu \approx 450$ Pa s, density $\rho_0 \approx 10^3$ kg/m³ and solutal diffusivity $D \approx 2.4 \times 10^{-4}$ mm²/s. This yields $Re \approx 1.6 \times 10^{-10}$ and $Pe \approx 0.3$, both of which are plausibly in the asymptotic regime. Moreover, using $\alpha c_\infty \approx 0.01$, the metabolic Rayleigh number at viscosity $\mu \approx 450$ Pa s is $Ra \approx 50$. Finally, for the specific model $\partial c/\partial n = -c/\ell$ proposed in Atis *et al.* (2019) with depletion length $\ell \approx 2$ mm, we estimate $\beta \approx R/\ell \approx 1.3$. This will depend on the specific form of γ , but suggests $\beta = O(1)$ in general.

Experimentally, the viscosity ranges over about three orders of magnitude and strongly influences the interfacial dynamics. We will therefore ultimately be interested in the dependence of the solution on the metabolic Rayleigh number Ra , which is inversely proportional to the viscosity. In the rest of this paper we assume all variables are dimensionless and we omit primes.

3. Boundary integral formulation

The three-dimensional system of equations above can, in principle, be studied analytically and/or solved numerically. However, the formulation couples PDEs defined on domains of different dimensions which significantly complicates analysis of the interfacial dynamics. Moreover, the formulation resists numerical solution as the bulk three-dimensional fluid must be discretized and coupled to a two-dimensional moving boundary problem on the surface. This is further complicated by the stress boundary condition on the open surface which generically results in singularities (Stephan 1987; Costabel *et al.* 2003). To circumvent these issues, in this section we reformulate the problem as an integro-differential equation defined solely on the microbial droplet.

3.1. Fourier space solution

Let $\mathbf{k} \in \mathbb{R}^2$ be a wavevector with magnitude $k = |\mathbf{k}|$. Taking the Fourier transform in the xy -plane of Eqs. (2.20)-(2.22), we find

$$-i \left(\frac{\mathbf{k}}{\partial_z} \right) \hat{P} + \left(-k^2 + \partial_z^2 \right) \hat{\mathbf{U}} - Ra \hat{c} \mathbf{e}_z = \mathbf{0}, \quad (3.1)$$

$$i \left(\frac{\mathbf{k}}{\partial_z} \right) \cdot \hat{\mathbf{U}} = 0, \quad (3.2)$$

$$\left(-k^2 + \partial_z^2 \right) \hat{c} = 0, \quad (3.3)$$

for $z < 0$, and where

$$(\hat{\mathbf{U}}, \hat{P}, \hat{c})(\mathbf{k}, z) = \int_{\mathbb{R}^2} (\mathbf{U}, P, c) e^{-i\mathbf{k} \cdot \mathbf{x}} d\mathbf{x} \quad (3.4)$$

denotes the Fourier transform with $\mathbf{x} \in \mathbb{R}^2$. This linear system of ODEs can be solved analytically. Decompose $\hat{\mathbf{U}}(\mathbf{k}, z) = (\hat{\mathbf{u}}, \hat{w})(\mathbf{k}, z)$ and define $\hat{\mathbf{u}}_0(\mathbf{k}) = \hat{\mathbf{u}}(\mathbf{k}, 0)$, $\hat{w}_0(\mathbf{k}) = \hat{w}(\mathbf{k}, 0)$, and $\hat{c}_0(\mathbf{k}) = \hat{c}(\mathbf{k}, 0)$. The no-penetration boundary condition $\mathbf{U} \cdot \mathbf{e}_z = 0$ implies

$\hat{w}_0 = 0$. The general solution, in terms of $\hat{\mathbf{u}}_0$ and \hat{c}_0 , for $\mathbf{k} \neq \mathbf{0}$, is then

$$\hat{c}(\mathbf{k}, z) = \hat{c}_0(\mathbf{k}) e^{kz}, \quad (3.5)$$

$$\hat{\mathbf{u}}(\mathbf{k}, z) = \left(\hat{\mathbf{u}}_0(\mathbf{k}) + \hat{\mathbf{u}}_1(\mathbf{k})z + \hat{\mathbf{u}}_2(\mathbf{k})z^2 \right) e^{kz}, \quad (3.6)$$

$$\hat{w}(\mathbf{k}, z) = \left(\hat{w}_1(\mathbf{k})z + \hat{w}_2(\mathbf{k})z^2 \right) e^{kz}, \quad (3.7)$$

$$\hat{P}(\mathbf{k}, z) = (\hat{P}_0(\mathbf{k}) + \hat{P}_1(\mathbf{k})z) e^{kz}, \quad (3.8)$$

where the coefficients are

$$\hat{P}_0(\mathbf{k}) = -2 \left((\mathbf{i}\mathbf{k} \cdot \hat{\mathbf{u}}_0) + \frac{3Ra\hat{c}_0}{8k} \right), \quad (3.9)$$

$$\hat{P}_1(\mathbf{k}) = -\frac{Ra\hat{c}_0}{2}, \quad (3.10)$$

$$\hat{\mathbf{u}}_1(\mathbf{k}) = -\frac{\mathbf{i}\mathbf{k}}{k} \left((\mathbf{i}\mathbf{k} \cdot \hat{\mathbf{u}}_0) + \frac{Ra\hat{c}_0}{4k} \right), \quad (3.11)$$

$$\hat{\mathbf{u}}_2(\mathbf{k}) = -\frac{\mathbf{i}\mathbf{k}}{8k} Ra\hat{c}_0, \quad (3.12)$$

$$\hat{w}_1(\mathbf{k}) = -(\mathbf{i}\mathbf{k} \cdot \hat{\mathbf{u}}_0), \quad (3.13)$$

$$\hat{w}_2(\mathbf{k}) = -\frac{Ra\hat{c}_0}{8}. \quad (3.14)$$

(Recall $z < 0$ so the Fourier coefficients decay in the far-field $z \rightarrow -\infty$.) Substituting this solution into the stress boundary condition $T[\mathbf{f}]|_{\mathcal{Q}} = -\nabla_{2D}p$, we find the balance between the surface velocity, concentration, and pressure,

$$\hat{\mathbf{u}}_0 = \mathbf{i}\mathbf{k} \left(-\frac{\widehat{\chi_{\mathcal{Q}} p}}{2k} + \frac{Ra}{8k^3} \hat{c}_0 \right), \quad (3.15)$$

where $\chi_{\mathcal{Q}}$ is the zero extension, namely

$$(\chi_{\mathcal{Q}}\nu)(\mathbf{x}) = \begin{cases} \nu(\mathbf{x}) & \mathbf{x} \in \mathcal{Q}, \\ 0 & \mathbf{x} \in S \setminus \mathcal{Q}. \end{cases} \quad (3.16)$$

It is important to note that this calculation requires $p = 0$ on $\partial\mathcal{Q}$. Specifically, in deriving the representation (3.15) we use

$$\begin{aligned} \frac{\partial \hat{\mathbf{u}}}{\partial z} \Big|_{z=0} &= - \int_{\mathcal{Q}} e^{-\mathbf{i}\mathbf{k} \cdot \mathbf{x}} \nabla_{2D} p \, d\mathbf{x} \\ &= + \int_{\mathcal{Q}} (-\mathbf{i}\mathbf{k}) e^{-\mathbf{i}\mathbf{k} \cdot \mathbf{x}} p \, d\mathbf{x} - \int_{\partial\mathcal{Q}} e^{-\mathbf{i}\mathbf{k} \cdot \boldsymbol{\Gamma}} p(\boldsymbol{\Gamma}) \, d\boldsymbol{\Gamma} \\ &= -\mathbf{i}\mathbf{k} \widehat{\chi_{\mathcal{Q}} p}, \end{aligned} \quad (3.17)$$

where the last equality requires $\int_{\partial\mathcal{Q}} e^{-\mathbf{i}\mathbf{k} \cdot \boldsymbol{\Gamma}} p(\boldsymbol{\Gamma}) \, d\boldsymbol{\Gamma} = 0$ for all $\mathbf{k} \in \mathbb{R}^2$ and hence $p(\boldsymbol{\Gamma}) = 0$.

3.2. An integro-differential equation

Equation (3.15) is expressed entirely in terms of quantities defined on the surface. However, the growth pressure is defined only on \mathcal{Q} while the concentration is defined on all of S . We

can further represent c by a function supported on Ω by choosing the representation

$$c(\mathbf{X}) = 1 - \frac{1}{4\pi} \int_{\Omega} \frac{\sigma(\mathbf{y})}{|\mathbf{X} - \mathbf{y}|} d\mathbf{y}, \quad (3.18)$$

where $\sigma : \Omega \rightarrow \mathbb{R}$ is an *a priori* unknown density. This expression is harmonic (i.e. $\Delta_{3D} c = 0$ in V), satisfies $\partial c / \partial z = 0$ on $S \setminus \Omega$, and obeys the far-field condition $c(\mathbf{X}) \rightarrow 1$ as $|\mathbf{X}| \rightarrow \infty$. The flux boundary condition $\partial c / \partial z|_{\Omega} = -\beta\gamma(c)$ can then be used to solve for σ . Specifically, noting that $\lim_{z \rightarrow 0} \partial_z \left(\int_{\Omega} \sigma(\mathbf{y}) / |(\mathbf{x}, z) - (\mathbf{y}, 0)| d\mathbf{y} \right) = 2\pi\sigma(\mathbf{x})$, we find an integral equation for σ , which may in general be nonlinear,

$$\frac{\sigma}{2} = \beta\gamma(1 - \mathcal{S}_{\Omega}[\sigma]) \quad \text{on } \Omega, \quad (3.19)$$

where

$$\mathcal{S}_{\Omega}[\nu](\mathbf{x}) = \frac{1}{4\pi} \int_{\Omega} \frac{\nu(\mathbf{y})}{|\mathbf{x} - \mathbf{y}|} d\mathbf{y} \quad (3.20)$$

is the single layer potential of the three-dimensional Laplacian. Taking the Fourier transform of (3.18) in the xy -plane for $\mathbf{k} \neq \mathbf{0}$ gives

$$\hat{c}_0(\mathbf{k}) = -\frac{1}{2k} \widehat{\chi_{\Omega}\sigma}(\mathbf{k}), \quad (3.21)$$

so that

$$\hat{\mathbf{u}}_0 = -ik \left(\frac{\widehat{\chi_{\Omega}p}}{2k} + \frac{Ra}{16k^4} \widehat{\chi_{\Omega}\sigma} \right). \quad (3.22)$$

Taking the inverse Fourier transform and applying the convolution theorem (see appendix B), we arrive at an integro-differential system of equations on Ω :

$$\mathbf{u} + \nabla_{2D} \left(\mathcal{S}_{\Omega}[p] + \frac{Ra}{16} \mathcal{B}_{\Omega,\kappa}[\sigma] \right) = \mathbf{0} \quad \text{in } \Omega, \quad (3.23)$$

$$\nabla_{2D} \cdot \mathbf{u} - \frac{\sigma}{2\beta} = 0 \quad \text{in } \Omega, \quad (3.24)$$

$$\sigma - 2\beta\gamma(1 - \mathcal{S}_{\Omega}[\sigma]) = 0 \quad \text{in } \Omega, \quad (3.25)$$

where

$$\mathcal{B}_{\Omega,\kappa}[\nu](\mathbf{x}) = \frac{1}{8\pi} \int_{\Omega} |\mathbf{x} - \mathbf{y}|^2 \left[\log \left(\frac{|\mathbf{x} - \mathbf{y}|}{R(\Omega)} \right) - 1 + \kappa \right] \nu(\mathbf{y}) d\mathbf{y} \quad (3.26)$$

is the volume potential of the two-dimensional bilaplacian Δ_{2D}^2 . Here $R(\Omega) = (|\Omega|/\pi)^{1/2}$ is a characteristic length scale and κ is an integration constant. (The term $-[1 + \log R(\Omega)]$ could be absorbed into the constant κ , however this choice will significantly simplify subsequent calculations.) The system (3.23)-(3.25) forms the complete set of integro-differential equations for the droplet velocity \mathbf{u} , growth pressure p , and density σ .

In this system, the density σ can be determined independently of \mathbf{u} and p from Eq. (3.25). Moreover, taking the divergence of (3.23) and using (3.24), we find

$$\mathcal{N}_{\Omega}[p] = - \left(\frac{\sigma}{2\beta} + \frac{Ra}{16} \mathcal{V}_{\Omega,\kappa}[\sigma] \right), \quad (3.27)$$

where the operators \mathcal{N}_Ω and $\mathcal{V}_{\Omega,\kappa}$ are

$$\mathcal{N}_\Omega[v](\mathbf{x}) := \Delta_{2D} \mathcal{S}_\Omega[v](\mathbf{x}) = \frac{1}{4\pi} \mathcal{f}_\Omega \frac{v(\mathbf{y})}{|\mathbf{x} - \mathbf{y}|^3} d\mathbf{y}, \quad (3.28)$$

$$\mathcal{V}_{\Omega,\kappa}[v](\mathbf{x}) := \Delta_{2D} \mathcal{B}_{\Omega,\kappa}[v](\mathbf{x}) = \frac{1}{2\pi} \int_\Omega \log \left(\frac{|\mathbf{x} - \mathbf{y}|}{R(\Omega)} + \kappa \right) v(\mathbf{y}) d\mathbf{y}, \quad (3.29)$$

which are the hypersingular operator and the volume potential of the two-dimensional Laplacian, respectively. Here \mathcal{f} denotes the Hadamard finite part integral. Given σ , Eq. (3.27) can then be solved for p , independently of the velocity. Finally, once p and σ are determined, the velocity is evaluated using Eq. (3.23). For the following, we will suppress the 2D subscript and use the notation $\nabla := \nabla_{2D}$ and $\Delta := \Delta_{2D}$. For simplicity we take $\kappa = 0$; the effect of this constant can be found in appendix C.

Before proceeding, it is interesting to note that the integro-differential formulation closely resembles models of tumor growth and proliferating cell collectives on rigid substrates (Greenspan 1976; Lowengrub *et al.* 2009; Weady *et al.* 2024). In the simplest case, these models take the form

$$\mathbf{u} + \nabla p = \mathbf{0} \quad \text{in } \Omega, \quad (3.30)$$

$$\nabla \cdot \mathbf{u} = \gamma \quad \text{in } \Omega, \quad (3.31)$$

$$p = 0 \quad \text{on } \partial\Omega. \quad (3.32)$$

The present model differs critically in that the growth-induced pressure acts non-locally through the integral operator.

4. Spectral analysis on the unit disk

The integral operators \mathcal{S}_Ω and \mathcal{N}_Ω of the previous section commonly arise in boundary integral methods for open surfaces. When that surface is the unit disk $D = \{\mathbf{x} \in \mathbb{R}^2 : |\mathbf{x}| < 1\}$, their spectral properties are well characterized. In this section we review some of these properties which will be particularly useful in our analysis. We refer to (Wolfe 1971; Boersma & Danick 1993; Martin 1996) for more thorough discussions.

4.1. Projected spherical harmonics

To start, we introduce the (complex) projected spherical harmonics, which in polar coordinates $\mathbf{x}(r, \theta) = r(\cos \theta, \sin \theta)^T$, $(r, \theta) \in [0, 1] \times [0, 2\pi)$, are given by

$$y_\ell^m(\mathbf{x}) = \sqrt{\frac{2\ell+1}{2\pi} \frac{(\ell-m)!}{(\ell+m)!}} P_\ell^m \left(\sqrt{1-r^2} \right) e^{im\theta}, \quad \ell \geq 0 \text{ and } |m| \leq \ell, \quad (4.1)$$

where P_ℓ^m are the associated Legendre polynomials. Defining the weight function $\omega(\mathbf{x}) = \sqrt{1 - |\mathbf{x}|^2}$, when $\ell_1 + m_1$ has the same parity as $\ell_2 + m_2$, these functions satisfy the orthogonality relation

$$\int_D \frac{y_{\ell_1}^{m_1*}(\mathbf{x}) y_{\ell_2}^{m_2}(\mathbf{x})}{\omega(\mathbf{x})} d\mathbf{x} = \delta_{\ell_1, \ell_2} \delta_{m_1, m_2}, \quad (4.2)$$

where $*$ denotes the complex conjugate. The subsets of functions with $\ell + m$ even/odd span two different spaces. Specifically, $\{y_\ell^m\}_{\ell+m \text{ even}}$ is an orthonormal basis for $C^\infty(D)$ while $\{y_\ell^m\}_{\ell+m \text{ odd}}$ is an orthonormal basis for the space $\{v(\mathbf{x}) : v(\mathbf{x})/\omega(\mathbf{x}) \in C^\infty(D)\}$.

4.2. Generalized eigenfunctions and eigenvalues

The functions y_ℓ^m with $\ell + m$ even and $\ell + m$ odd are generalized eigenfunctions of the operators \mathcal{S}_D and \mathcal{N}_D , respectively,

$$\mathcal{S}_D \left[\frac{y_\ell^m}{\omega} \right] (\mathbf{x}) = \frac{\lambda_\ell^m}{4} y_\ell^m(\mathbf{x}), \quad \ell + m \text{ even}, \quad (4.3)$$

$$\mathcal{N}_D [y_\ell^m] (\mathbf{x}) = -\frac{1}{\lambda_\ell^m} \frac{y_\ell^m(\mathbf{x})}{\omega(\mathbf{x})}, \quad \ell + m \text{ odd}, \quad (4.4)$$

with generalized eigenvalues given by

$$\lambda_\ell^m = \frac{\Gamma\left(\frac{\ell+m}{2} + \frac{1}{2}\right)}{\Gamma\left(\frac{\ell+m}{2} + 1\right)} \frac{\Gamma\left(\frac{\ell-m}{2} + \frac{1}{2}\right)}{\Gamma\left(\frac{\ell-m}{2} + 1\right)}, \quad (4.5)$$

where Γ is the gamma function. Note that equations (4.3) and (4.4) imply \mathcal{S}_D maps function with $1/\omega(\mathbf{x})$ singularities to smooth functions, and \mathcal{N}_D maps functions that go to 0 as $\omega(\mathbf{x})$ for $|\mathbf{x}| \rightarrow 1$ to smooth functions.

4.3. Special cases

In our analysis, we will often encounter the specific functions y_m^m and y_{m+1}^m . For the former, using the fact that $P_m^m(\sqrt{1-r^2}) \propto r^m$, we find

$$y_m^m(\mathbf{x}) \propto r^m e^{im\theta}. \quad (4.6)$$

Next, using the recursion relation $P_{m+1}^m(x) = (2m+1)xP_m^m(x)$, we find

$$y_{m+1}^m(\mathbf{x}) \propto \sqrt{1-r^2} r^m e^{im\theta}. \quad (4.7)$$

We will also need the products $(1-r^2)r^m$, $(1-r^2)^{3/2}r^m$, $(1-r^2)^2r^m$ in terms of P_ℓ^m polynomials, which can be found in appendix D. These relations also yield identities for the integral operators,

$$\mathcal{S}_D [\omega(\zeta') \zeta'^j] = \left(\frac{\lambda_j^j - \lambda_{j+1}^{j+1} |\zeta'|^2}{8} \right) \zeta^j, \quad (4.8)$$

$$\mathcal{S}_D [\omega^3(\zeta') \zeta'^j] = \frac{3}{32} \left(\lambda_j^j - 2\lambda_{j+1}^{j+1} |\zeta'|^2 + \lambda_{j+2}^{j+2} |\zeta'|^4 \right) \zeta^j, \quad (4.9)$$

and

$$\mathcal{N}_D [\omega(\zeta') \zeta'^j] = -\frac{1}{\lambda_{j+1}^j} \zeta^j, \quad (4.10)$$

$$\mathcal{N}_D [\omega^3(\zeta') \zeta'^j] = \frac{3}{4\lambda_{j+1}^j} \left(-2 + \left(2 + \frac{1}{j+1} \right) |\zeta'|^2 \right) \zeta^j. \quad (4.11)$$

Finally, the eigenvalues satisfy the sum conditions

$$\sum_{j=0}^m \lambda_j^j = (2m+1) \lambda_m^m, \quad (4.12)$$

and

$$\sum_{j=0}^m \frac{1}{\lambda_{j+1}^j} = \frac{(2m+3)}{3\lambda_{m+1}^m}, \quad (4.13)$$

which are straightforward to prove through induction.

5. Axisymmetric solutions

Taking advantage of the spectral properties discussed in section 4, we now seek axisymmetric solutions to the system of integro-differential equations (3.23)-(3.25) on the disk of radius R , denoted by $D_R = \{\mathbf{x} \in \mathbb{R}^2 : |\mathbf{x}| < R\}$. For simplicity, we assume we are in the nutrient-rich regime so that $\gamma(c) = 1$. While this *a priori* violates the physical constraint $\gamma(0) = 0$, this approximation is valid so long as the concentration is everywhere positive. Indeed, using the representation (3.18), one can show this holds for $\beta < 1/R$ when $\Omega = D_R$. We individually solve the problems for growth-dominated flow ($Ra = 0$) and buoyancy-dominated flow ($Ra \rightarrow \infty$) from which we can construct the solution for general Ra .

5.1. Growth

We first consider the case of growth-dominated flow, $Ra = 0$, for which the system of equations reduces to

$$\mathbf{u}_g + \nabla S_{D_R}[p_g] = \mathbf{0}, \quad (5.1)$$

$$\mathcal{N}_{D_R}[p_g] + 1 = 0. \quad (5.2)$$

Making the change of variables $\mathbf{x} = Rx'$, $\mathbf{u}_g = R\mathbf{u}'_g$ and $p_g = Rp'_g$, the equations transform to

$$\mathbf{u}'_g + \nabla' S_D[p'_g] = \mathbf{0}, \quad (5.3)$$

$$\mathcal{N}_D[p'_g] + 1 = 0. \quad (5.4)$$

These equations are independent of R , implying the solution for (\mathbf{u}_g, p_g) is homogeneous in R . Noting that $y_1^0 \propto \omega$ and using the property $\mathcal{N}_D[y_\ell^m] = -y_\ell^m/(\lambda_\ell^m \omega)$, the scaled pressure is given by

$$p'_g(\mathbf{x}') = \lambda_1^0 \sqrt{1 - |\mathbf{x}'|^2}. \quad (5.5)$$

We can in principle evaluate $S_D[p'_g]$ to compute \mathbf{u}'_g . However, under the assumption of axisymmetry, the velocity can be derived directly from the condition $\nabla' \cdot \mathbf{u}'_g = 1$ so that

$$\mathbf{u}'_g(\mathbf{x}') = \frac{\mathbf{x}'}{2}. \quad (5.6)$$

5.2. Buoyancy

We next consider the limit of buoyancy-dominated flow $Ra \rightarrow \infty$. Defining $\mathbf{u} = (\beta Ra)\mathbf{u}_b$, $p = (\beta Ra)p_b$, and $\sigma = \beta\sigma_b$ and taking $Ra \rightarrow \infty$, the system of equations is

$$\mathbf{u}_b + \nabla S_{D_R}[p_b] + \frac{1}{16} \nabla \mathcal{B}_{D_R}[\sigma_b] = \mathbf{0}, \quad (5.7)$$

$$\mathcal{N}_{D_R}[p_b] + \frac{1}{16} \mathcal{V}_{D_R}[\sigma_b] = 0, \quad (5.8)$$

$$\sigma_b - 2 = 0. \quad (5.9)$$

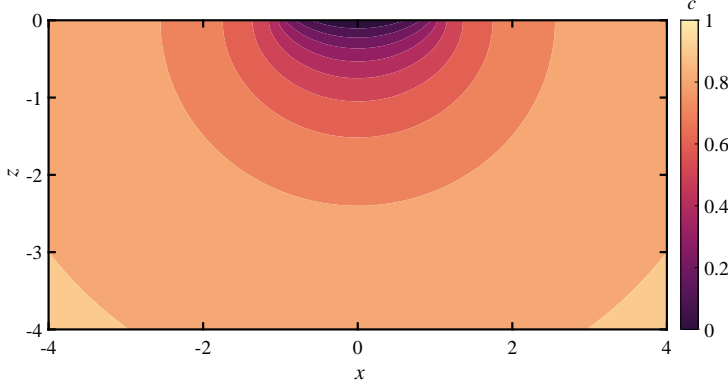


Figure 2. Axisymmetric solution for the nutrient concentration field. Nutrients are depleted near the droplet and the concentration increases in concentric ellipsoidal-like contours which become increasingly circular.

Again defining $\mathbf{x} = Rx'$, $\mathbf{u}_b = R^3 \mathbf{u}'_b$, $p_b = R^3 p'_b$, and $\sigma_b = \sigma'_b$, we get

$$\mathbf{u}'_b + \nabla' \mathcal{S}_D[p'_b] + \frac{1}{16} \nabla' \mathcal{B}_D[\sigma'_b] = \mathbf{0}, \quad (5.10)$$

$$\mathcal{N}_D[p'_b] + \frac{1}{16} \mathcal{V}_D[\sigma'_b] = 0, \quad (5.11)$$

$$\sigma'_b - 2 = 0, \quad (5.12)$$

which is independent of R .

Now trivially we have $\sigma'_b(\mathbf{x}') = 2$, which we can use to numerically evaluate the concentration field in the bulk V . A cross-sectional view of the corresponding concentration field is shown in Fig. 2, where we see nutrient is depleted in the vicinity of the droplet and increases outward in the form of concentric ellipsoidal-like contours which become increasingly circular at far distances.

To compute the pressure, we need to evaluate $\mathcal{V}_D[\sigma'_b]$. Using Eq. (E5), we find

$$\mathcal{V}_D[\sigma'_b](\mathbf{x}') = \frac{|\mathbf{x}'|^2 - 1}{2}. \quad (5.13)$$

The pressure therefore solves the equation

$$\mathcal{N}_D[p'_b](\mathbf{x}') = -\left(\frac{|\mathbf{x}'|^2 - 1}{2}\right). \quad (5.14)$$

Using the identities (4.10) and (4.11), we find

$$p'_b(\mathbf{x}') = -\frac{\lambda_1^0 \sqrt{1 - |\mathbf{x}'|^2}}{96} \left(1 + \frac{4}{3}(1 - |\mathbf{x}'|^2)\right). \quad (5.15)$$

Finally, as before, the axisymmetric velocity can be determined directly from the condition $\nabla' \cdot \mathbf{u}'_b = 0$, from which we immediately see $\mathbf{u}'_b = \mathbf{0}$ in D .

5.3. General axisymmetric solution

For pure growth ($Ra = 0$) we found $\mathbf{u}_g = R\mathbf{u}'_g$ and $p_g = Rp'_g$, where (\mathbf{u}'_g, p'_g) are the solution on the unit disk. For buoyancy-dominated flow ($Ra \rightarrow \infty$), we found $\mathbf{u}_b = R^3 \mathbf{u}'_b$ and $p_b = R^3 p'_b$ where (\mathbf{u}'_b, p'_b) are the solution on the unit disk with unit Ra , unit β , and a

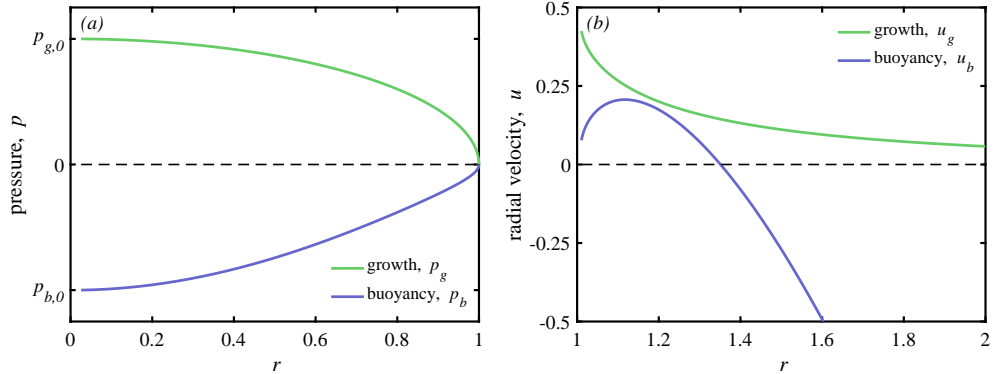


Figure 3. (a) Axisymmetric pressure on the unit disk for growth-dominated flow (green) and buoyancy-dominated flow (purple), each scaled by their value at the origin ($p_{g,0} \approx 1.27$ and $p_{b,0} \approx -0.031$) for visualization. The former is strictly positive while the latter is strictly negative. (b) Radial velocity for growth-dominated flow (green) and buoyancy-dominated flow (purple) exterior to the droplet. The former is strictly positive and monotonically decreasing while the latter exhibits a local maximum near $r \approx 1.1$.

divergence-free velocity. The general solution for the disk of radius R may then be written

$$p(\mathbf{x}) = Rp'_g(\mathbf{x}/R) + \beta RaR^3 p'_b(\mathbf{x}/R). \quad (5.16)$$

along with the velocity

$$\mathbf{u}(\mathbf{x}) = \frac{\mathbf{x}}{2}. \quad (5.17)$$

From the kinematic boundary condition (2.14), this shows this axisymmetric solution is a radially expanding disk whose radius grows exponentially in time, $R(t) = R(0)e^{t/2}$.

Figure 3(a) shows the axisymmetric pressure due to growth p_g and buoyancy p_b on the unit disk with $\beta = 1$, scaled by the magnitude of their values at the origin for visualization ($p_{g,0} \approx 1.27$ and $p_{b,0} \approx -0.031$). The former is strictly positive while the latter is strictly negative. Thus, as the Rayleigh number increases, the pressure will eventually take on negative values. Moreover, the pressure becomes negative everywhere inside D when $\beta Ra = 96$.

The radial velocity on the surface outside of the disk for both growth- and buoyancy-dominated flow, evaluated numerically, is shown in Fig. 3(b). For visualization, the buoyancy-dominated flow is scaled by a factor of 96. For growth-dominated flow, the velocity decreases monotonically from $u_g = 1/2$ at $r = 1$, consistent with continuity of the velocity, towards $u_g \rightarrow 0$ as $r \rightarrow \infty$. The scaling here is $O(1/r^2)$ owing to the $1/r$ kernel in \mathcal{S}_D . For buoyancy-dominated flow, the velocity initially increases from $u_b = 0$ at $r = 1$, again consistent with continuity, and later decreases after reaching a maximum at $r \approx 1.1$. This maximum is also observed in experiments (Atis *et al.* 2019). The velocity in this case eventually takes on negative values and scales as $u = O(r \log r)$ owing to the kernel in the operator \mathcal{B}_D . This nonphysical divergence of the velocity is similar to the Stokes paradox and arises from the zero Re and Pe approximation on an unbounded domain. Hence the solution should be interpreted as an inner solution which is matched to an outer solution by the free constant κ in the operators $\mathcal{B}_{Q,\kappa}$ and $\mathcal{V}_{Q,\kappa}$.

A cross sectional view of the streamlines and velocity field in the bulk is shown in Fig. 4 for (a) growth-dominated flow and (b) buoyancy-dominated flow. The formulation used for these computations is described in appendix B. The flow field in the growth-dominated regime resembles a stagnation point flow, where fluid is pulled from beneath the droplet

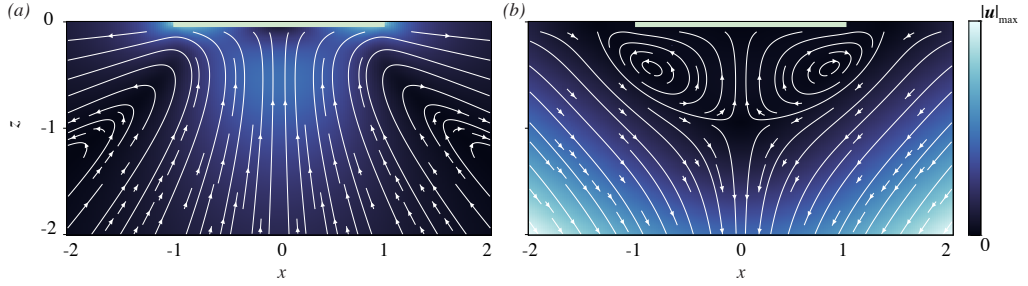


Figure 4. Cross-sectional streamlines and velocity magnitude in the (a) growth-dominated regime ($Ra = 0$) and (b) buoyancy-dominated regime ($Ra \rightarrow \infty$). In the former, fluid is pulled from below and pushed outward, reminiscent of stagnation point flow. In the latter, a vortex ring forms below the droplet, with the core positioned near the droplet edge.

and pushed outward at the surface. The character of the flow changes significantly in the buoyancy-dominated regime, where a vortex ring forms beneath the droplet. This vortex ring extends slightly beyond the droplet, with its core located near the droplet boundary. Note that the extent of this vortex ring is modified by the constant κ , which sets the position of the lower stagnation point.

6. Linear stability analysis

In this section, we analyze the geometric stability of the axisymmetric solution with $\gamma(c) = 1$ at short times. To assess the evolution of small perturbations to this solution, we make an Ansatz for a parameterization of the boundary $\partial\mathcal{Q}_\varepsilon^m(t)$ of the perturbed domain $\mathcal{Q}_\varepsilon^m(t)$,

$$\mathbf{I}^m(\theta, t) = R(t) \left[(1 + \varepsilon(t) \cos(m\theta)) \hat{\mathbf{r}} + \varepsilon(t) \sin(m\theta) \hat{\theta} \right], \quad \text{for } \theta \in [0, 2\pi), \quad (6.1)$$

where $\varepsilon(t) \ll 1$ is the perturbation amplitude, m is the perturbation frequency, and $\hat{\mathbf{r}} = (\cos \theta, \sin \theta)^T$ and $\hat{\theta} = (-\sin \theta, \cos \theta)^T$ are basis vectors. We will show that, under a suitable tangential velocity which does not affect the geometry, this Ansatz is preserved up to $O(\varepsilon^2)$. As in the axisymmetric solution, we separate our analysis into the growth-dominated ($Ra = 0$) and buoyancy-dominated ($Ra \rightarrow \infty$) regimes from which we can reconstruct the solution for general Ra .

6.1. Representation on the unit disk

Because we are considering geometric deformations and the integral operators depend on the domain, it is critical to define the equations over a fixed reference domain, which we take to be the unit disk $D = \{\xi \in \mathbb{R}^2 : |\xi| = 1\}$. To this end, let $f : D \rightarrow \Omega$ be an invertible mapping and let $\tilde{\mathbf{e}}_i(\xi) = \partial f / \partial \xi_i$ be the associated (unnormalized) basis vectors for $i = 1, 2$, where $\xi = (\xi_1, \xi_2) \in D$. This yields the metric tensor $(\mathbf{G}_f)_{ij} = \tilde{\mathbf{e}}_i \cdot \tilde{\mathbf{e}}_j$ and Jacobian $J_f(\xi) = \sqrt{\det \mathbf{G}_f(\xi)}$. The system of equations is then

$$\tilde{\mathbf{u}} + \mathbf{G}_f^{-1} \left(\tilde{\nabla} \mathcal{S}_f[p] + \frac{Ra}{16} \tilde{\nabla} \mathcal{B}_f[\sigma] \right) = \mathbf{0} \quad \text{in } D, \quad (6.2)$$

$$J_f^{-1} \tilde{\nabla} \cdot (J_f \tilde{\mathbf{u}}) - \frac{\sigma}{2\beta} = 0 \quad \text{in } D, \quad (6.3)$$

$$\sigma - 2\beta = 0 \quad \text{in } D, \quad (6.4)$$

where $\tilde{\mathbf{u}} = (\tilde{u}_1, \tilde{u}_2)$ is expressed in the basis $\tilde{\mathbf{e}}_1, \tilde{\mathbf{e}}_2$ such that $\mathbf{u} = \tilde{u}_1 \tilde{\mathbf{e}}_1 + \tilde{u}_2 \tilde{\mathbf{e}}_2$ and $\tilde{\nabla}$ denotes the gradient operator on D . The transformed integral operators are

$$\mathcal{S}_f[v](\xi) = \frac{1}{4\pi} \int_D \frac{1}{|f(\xi) - f(\xi')|} (v \circ f)(\xi') J_f(\xi') d\xi', \quad (6.5)$$

$$\mathcal{B}_f[v](\xi) = \frac{1}{8\pi} \int_D |f(\xi) - f(\xi')|^2 \left[\log \left(\frac{|f(\xi) - f(\xi')|}{R(\mathcal{Q})} \right) - 1 \right] (v \circ f)(\xi') J_f(\xi') d\xi'. \quad (6.6)$$

Similarly, the pressure satisfies

$$\mathcal{N}_f[p] = - \left(\frac{\sigma}{2\beta} + \frac{Ra}{16} \mathcal{V}_f[\sigma] \right), \quad (6.7)$$

where

$$\mathcal{N}_f[v](\xi) = \frac{1}{4\pi} \int_D \frac{1}{|f(\xi) - f(\xi')|^3} (v \circ f)(\xi') J_f(\xi') d\xi', \quad (6.8)$$

$$\mathcal{V}_f[v](\xi) = \frac{1}{2\pi} \int_D \log \left(\frac{|f(\xi) - f(\xi')|}{R(\mathcal{Q})} \right) (v \circ f)(\xi') J_f(\xi') d\xi'. \quad (6.9)$$

While in principle f can be any invertible map, it is particularly advantageous to choose it to be conformal so that $\mathbf{G}_f(\xi) = J_f(\xi) \mathbf{I}$. This choice allows us to introduce the complex variable $\zeta = \xi_1 + i\xi_2$ associated to the point $\xi = (\xi_1, \xi_2) \in D$ and the associated complex-valued conformal map $f : D \rightarrow \mathcal{Q}$. Moreover, it preserves the form of the singularities in the kernel, allowing us to compute shape derivatives (Martin 1996). Geometrically, the conformal map also preserves angles so that the normal component of \mathbf{u} is preserved, i.e.

$$(\mathbf{u} \cdot \hat{\mathbf{n}})(f(e^{i\theta})) = (J_f^{1/2} \tilde{\mathbf{u}} \cdot \hat{\mathbf{r}})(e^{i\theta}). \quad (6.10)$$

It is readily seen that

$$f_{R,\varepsilon}^m(\zeta, t) = R(t)[\zeta + \varepsilon(t)\zeta^{m+1}] \quad (6.11)$$

is a conformal map from D to $\mathcal{Q}_\varepsilon^m(t)$. The associated basis functions may then be expressed in the polar coordinate system $\zeta = re^{i\theta}$ as

$$\tilde{\mathbf{e}}_r = R \left[(1 + \varepsilon(m+1)r^m \cos m\theta) \hat{\mathbf{r}} + \varepsilon(m+1)r^m \sin m\theta \hat{\theta} \right], \quad (6.12)$$

$$\tilde{\mathbf{e}}_\theta = R \left[-\varepsilon(m+1)r^{m+1} \sin m\theta \hat{\mathbf{r}} + (1 + \varepsilon(m+1)r^{m+1} \cos m\theta) \hat{\theta} \right], \quad (6.13)$$

which notably scale in proportion to R . The normal vector, in terms of θ , is then

$$\hat{\mathbf{n}} = \frac{\tilde{\mathbf{e}}_r}{|\tilde{\mathbf{e}}_r|} \Big|_{r=1} = \hat{\mathbf{r}} + \varepsilon(m+1) \sin m\theta \hat{\theta} + O(\varepsilon^2). \quad (6.14)$$

We similarly define the scaling transformation $f_R(\zeta, t) = R(t)\zeta$, which describes the radially expanding base state.

6.2. Linearization

In the following analysis we will need the shape derivative, with respect to ε , of the Jacobian and the integral operators induced by the conformal map. We will use the natural complexification for which complex-valued functions are interpreted as their real part. The Jacobian is straightforward,

$$\delta J_{D_R}^m = \lim_{\varepsilon \rightarrow 0} \frac{J_{f_{R,\varepsilon}^m} - J_{f_R}}{\varepsilon} = 2(m+1)R^2 \zeta^m. \quad (6.15)$$

For an integral operator $\mathcal{T}_{f_{R,\varepsilon}}^m$, we adopt the following notation for the shape derivative with respect to ε at fixed R ,

$$\delta\mathcal{T}_{D_R}^m[v] = \lim_{\varepsilon \rightarrow 0} \frac{\mathcal{T}_{f_{R,\varepsilon}}^m \left[v \circ \left(f_{R,\varepsilon}^m \right)^{-1} \right] - \mathcal{T}_{f_R} \left[v \circ f_R^{-1} \right]}{\varepsilon}. \quad (6.16)$$

Using the identity

$$\frac{f_{R,\varepsilon}^m(\zeta) - f_{R,\varepsilon}^m(\zeta')}{\zeta - \zeta'} = R \left(1 + \varepsilon \sum_{j=0}^m \zeta^j \zeta'^{m-j} \right) + O(\varepsilon^2), \quad (6.17)$$

a straightforward, but technical, calculation gives

$$\delta\mathcal{S}_{D_R}^m[v](\zeta) = R \left[2(m+1)\mathcal{S}_D[\zeta'^m v(\zeta')] - \mathcal{S}_D[C_m(\zeta, \zeta')v(\zeta')] \right], \quad (6.18)$$

$$\delta\mathcal{N}_{D_R}^m[v](\zeta) = R^{-1} \left[2(m+1)\mathcal{N}_D[\zeta'^m v(\zeta')] - 3\mathcal{N}_D[C_m(\zeta, \zeta')v(\zeta')](\zeta) \right], \quad (6.19)$$

$$\delta\mathcal{V}_{D_R}^m[v](\zeta) = R^2 \left[2(m+1)\mathcal{V}_D[\zeta'^m v(\zeta')] + \mathcal{I}_{D,0}[C_m(\zeta, \zeta')v(\zeta')] \right], \quad (6.20)$$

$$\begin{aligned} \delta\mathcal{B}_{D_R}^m[v](\zeta) = R^4 & \left[2(m+1)\mathcal{B}_D[\zeta'^m v(\zeta')] + 2\mathcal{B}_D[C_m(\zeta, \zeta')v(\zeta')] \right. \\ & \left. + (1/4)\mathcal{I}_{D,2}[C_m(\zeta, \zeta')v(\zeta')] \right], \end{aligned} \quad (6.21)$$

where

$$C_m(\zeta, \zeta') = \sum_{j=0}^m \zeta^j \zeta'^{m-j} \quad (6.22)$$

and

$$\mathcal{I}_{D,k}[v] = \frac{1}{2\pi} \int_D |\zeta - \zeta'|^k v(\zeta') d\zeta'. \quad (6.23)$$

For a function of two variables $v(\zeta, \zeta')$ and integral operator \mathcal{T}_D with kernel $K(\zeta - \zeta')$, we use the slight abuse of notation

$$\mathcal{T}_D[v(\zeta, \zeta')](\zeta) = \int_D K(\zeta - \zeta') v(\zeta, \zeta') d\zeta', \quad (6.24)$$

where primed variables always denote the integration variable.

6.3. Growth

We first analyze the stability of growth-dominated flow, $Ra = 0$. Here the system of equations on the reference domain, using the concentration density $\sigma(\mathbf{x}) = 2$, is

$$\tilde{\mathbf{u}}_g + J_{f_{R,\varepsilon}}^{-1} \tilde{\nabla} \mathcal{S}_{f_{R,\varepsilon}}^m[p_g] = \mathbf{0}, \quad (6.25)$$

$$\mathcal{N}_{f_{R,\varepsilon}}^m[p_g] + 1 = 0. \quad (6.26)$$

We assume a regular perturbation expansion for each variable,

$$\tilde{\mathbf{u}}_g = \tilde{\mathbf{u}}_0 + \varepsilon \tilde{\mathbf{u}}_1 + O(\varepsilon^2), \quad (6.27)$$

$$(p_g \circ f_{R,\varepsilon}^m) = R(p_0 + \varepsilon p_1) + O(\varepsilon^2). \quad (6.28)$$

(Recall $\tilde{\mathbf{u}}$ is expressed in the unnormalized basis so that $\mathbf{u} = \tilde{u}_1 \tilde{\mathbf{e}}_1 + \tilde{u}_2 \tilde{\mathbf{e}}_2$ scales with R .) Substituting above and matching powers of ε , the $O(1)$ equations are given by the unit disk

equations

$$\tilde{\mathbf{u}}_0 + \tilde{\nabla} \mathcal{S}_D[p_0] = \mathbf{0}, \quad (6.29)$$

$$\mathcal{N}_D[p_0] + 1 = 0, \quad (6.30)$$

and the $O(\varepsilon)$ equations are

$$\tilde{\mathbf{u}}_1 + \delta \mathcal{J}_D^m \tilde{\mathbf{u}}_0 + \tilde{\nabla} \mathcal{S}_D[p_1] + \tilde{\nabla} \delta \mathcal{S}_D^m[p_0] = \mathbf{0}, \quad (6.31)$$

$$\mathcal{N}_D[p_1] + \delta \mathcal{N}_D^m[p_0] = 0, \quad (6.32)$$

where we used $\tilde{\mathbf{u}}_0 + \tilde{\nabla} \mathcal{S}_D[p_0] = \mathbf{0}$ from the $O(1)$ equation.

To compute the $O(\varepsilon)$ pressure p_1 , we will need to evaluate $\delta \mathcal{N}_D^m[p_0]$. In section 5, we showed $p_0(\zeta) = \lambda_1^0 \omega(\zeta)$. Using the identities (4.10) and (4.13), we find

$$\delta \mathcal{N}_D^m[p_0] = -\frac{\lambda_1^0}{\lambda_{m+1}^m} \zeta^m. \quad (6.33)$$

From this, using the fact that $y_{m+1}^m(\zeta) \propto \omega(\zeta) \zeta^m$, we can solve Eq. (6.32) for p_1 ,

$$p_1(\zeta) = \lambda_1^0 \omega(\zeta) \zeta^m. \quad (6.34)$$

To determine the velocity, we need to evaluate $\mathcal{S}_D[p_1]$ and $\delta \mathcal{S}_D^m[p_0]$. The identity (4.8) directly gives

$$\mathcal{S}_D[p_1] = \lambda_1^0 \left(\frac{\lambda_m^m - \lambda_{m+1}^{m+1} |\zeta|^2}{8} \right) \zeta^m. \quad (6.35)$$

Finally, using (4.8) and (4.12) we find

$$\delta \mathcal{S}_D^m[p_0] = \lambda_1^0 \left(\frac{\lambda_m^m - (\lambda_0^0 - \lambda_{m+1}^{m+1}) |\zeta|^2}{8} \right) \zeta^m. \quad (6.36)$$

This yields the $O(\varepsilon)$ interface velocity

$$\begin{aligned} (\tilde{\mathbf{u}}_1 \cdot \hat{\mathbf{r}})(e^{i\theta}) &= -\text{Re} \left[(m+1) \zeta^m (\tilde{\mathbf{u}}_0 \cdot \hat{\mathbf{r}}) + \frac{\partial}{\partial r} (\mathcal{S}_D[p_1] + \delta \mathcal{S}_D^m[p_0]) \right] \Big|_{\zeta=e^{i\theta}} \\ &= \left(\frac{1}{2} - m \frac{\lambda_1^0 \lambda_m^m}{4} \right) \cos m\theta \\ &=: \sigma_g^m \cos m\theta. \end{aligned} \quad (6.37)$$

Values of the coefficient σ_g^m greater than 1/2 indicate that perturbations are amplified while negative values indicate they are suppressed. (Note that σ_g^m is not strictly the growth rate associated with the perturbation owing to the growing domain; see Eq. (6.63) for an explicit characterization.) A plot of σ_g^m is shown in Fig. 5. The $m = 0$ mode has $\sigma_g^m = 1/2$ and reflects a dilation. The $m = 1$ mode has $\sigma_g^m = 0$, which is consistent with translational invariance. All other modes are negative, showing growth has a stabilizing effect. For large m we find $\sigma_g^m = O(m^{1/2})$, which can readily be derived from the identity $\lambda_m^m = \Gamma(m + \frac{1}{2}) \Gamma(1/2) / \Gamma(m+1)$ along with the asymptotic scaling $\Gamma(x+1) / \Gamma(x+s) \sim x^{1-s}$.

It is also interesting to compare this scaling to that of a colony growing on a rigid substrate (3.30)-(3.32), in which the growth pressure acts locally. Linear stability analysis of this simpler model, which is included in appendix F, gives $\sigma_{g,\text{rigid}}^m = -(m-1)/2$. This

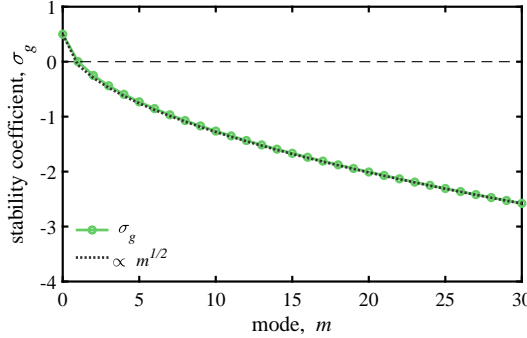


Figure 5. Stability coefficient σ_g^m for growth-dominated flow ($Ra = 0$). For $m = 0$, which corresponds to a dilation, the coefficient is $\sigma_g^0 = 1/2$, consistent with the $O(1)$ solution $R(t) = R_0 e^{t/2}$. For $m = 1$ we have $\sigma_g^1 = 0$, which is reflective of translational invariance. All other coefficients are negative, indicating that growth is stabilizing, and tend towards negative infinity as $O(m^{1/2})$.

is also linearly stable but has a linear scaling with respect to m . In this case we expect perturbations to be suppressed at a faster rate. Notably, the quantitative stabilizing behavior for growth on a viscous substrate is not captured by the local pressure model.

6.4. Buoyancy

We next analyze the stability of buoyancy dominated flow, $Ra \rightarrow \infty$. Defining $\tilde{\mathbf{u}} = (\beta Ra)\mathbf{\tilde{u}}_b$, $p = (\beta Ra)p_b$, and $\sigma = \beta\sigma_b$ and taking $Ra \rightarrow \infty$, the system of equations is

$$\tilde{\mathbf{u}}_b + J_{f_{R,\varepsilon}^m}^{-1} \left(\tilde{\nabla} \mathcal{S}_{f_{R,\varepsilon}^m} [p_b] + \frac{1}{16} \tilde{\nabla} \mathcal{B}_{f_{R,\varepsilon}^m} [\sigma_b] \right) = \mathbf{0}, \quad (6.38)$$

$$\mathcal{N}_{f_{R,\varepsilon}^m} [p_b] + \frac{1}{16} \mathcal{V}_{f_{R,\varepsilon}^m} [\sigma_b] = 0, \quad (6.39)$$

$$\sigma_b - 2 = 0. \quad (6.40)$$

Similar to before, we expand

$$\tilde{\mathbf{u}}_b = R^2 (\tilde{\mathbf{u}}_0 + \varepsilon \tilde{\mathbf{u}}_1) + O(\varepsilon^2), \quad (6.41)$$

$$p_b \circ f_{R,\varepsilon}^m = R^3 (p_0 + \varepsilon p_1) + O(\varepsilon^2), \quad (6.42)$$

$$\sigma_b \circ f_{R,\varepsilon}^m = (\sigma_0 + \varepsilon \sigma_1) + O(\varepsilon^2). \quad (6.43)$$

Substituting above and matching powers of ε , the $O(1)$ equations are given by the unit disk equations

$$\tilde{\mathbf{u}}_0 + \tilde{\nabla} \mathcal{S}_D [p_0] + \frac{1}{16} \tilde{\nabla} \mathcal{B}_D [\sigma_0] = \mathbf{0}, \quad (6.44)$$

$$\mathcal{N}_D [p_0] + \frac{1}{16} \mathcal{V}_D [\sigma_0] = 0, \quad (6.45)$$

$$\sigma_0 - 2 = 0, \quad (6.46)$$

and the $O(\varepsilon)$ equations are

$$\tilde{\mathbf{u}}_1 + \tilde{\nabla} \left(\mathcal{S}_D[p_1] + \delta \mathcal{S}_D^m[p_0] \right) + \frac{1}{16} \tilde{\nabla} \left(\mathcal{B}_D[\sigma_1] + \delta \mathcal{B}_D^m[\sigma_0] \right) = \mathbf{0}, \quad (6.47)$$

$$\mathcal{N}_D[p_1] + \delta \mathcal{N}_D^m[p_0] + \frac{1}{16} \left(\mathcal{V}_D[\sigma_1] + \delta \mathcal{V}_D^m[\sigma_0] \right) = 0, \quad (6.48)$$

$$\sigma_1 = 0. \quad (6.49)$$

Note that we used $\tilde{\mathbf{u}}_0 + \tilde{\nabla}(\mathcal{S}_D[p_0] + (1/16)\mathcal{B}_D[\sigma_0]) = \mathbf{0}$ from the $O(1)$ equation to simplify the first equation. In the following we assume $m \geq 1$; the case $m = 0$ is trivial.

The $O(1)$ solution p_0 is given by Eq. (5.15) and we trivially have $\sigma_0 = 2$ and $\sigma_1 = 0$. In order to compute the perturbed pressure p_1 , we must first evaluate $\delta \mathcal{N}_D^m[p_0]$ and $\delta \mathcal{V}_D^m[\sigma_0]$. Using identities (4.10), (4.11), and (4.13), we find

$$\delta \mathcal{N}_D^m[p_0] = \left[\frac{\lambda_1^0}{32(m+1)\lambda_{m+1}^m} \left((m+2) - (2m+3)(1-|\zeta|^2) \right) - \frac{1}{16} |\zeta|^2 \right] \zeta^m. \quad (6.50)$$

Using the identity (E 5) for $m \geq 1$, we have

$$\delta \mathcal{V}_D^m[\sigma_0] = \left(|\zeta|^2 - \frac{1}{m} \right) \zeta^m. \quad (6.51)$$

We can then use Eq. (6.48) to solve for p_1 ,

$$p_1(\zeta) = \frac{\lambda_1^0}{96} \left(3 - \frac{6\lambda_{m+1}^m}{m\lambda_1^0} - 4(1-|\zeta|^2) \right) \omega(\zeta) \zeta^m. \quad (6.52)$$

To compute the velocity, we need to evaluate $\mathcal{S}_D[p_1]$, $\delta \mathcal{S}_D^m[p_0]$, and $\delta \mathcal{B}_D^m[\sigma_0]$. Using the identities (4.8), (4.9), and (4.12), we get

$$\mathcal{S}_D[p_1] = \frac{3}{768} \left[\lambda_1^0 \left(\lambda_{m+1}^{m+1} |\zeta|^2 - \lambda_{m+2}^{m+2} |\zeta|^4 \right) - \frac{4}{m} \left(\frac{2}{2m+1} - \frac{|\zeta|^2}{m+1} \right) \right] \zeta^m, \quad (6.53)$$

$$\delta \mathcal{S}_D^m[p_0] = \frac{1}{768} \left[\lambda_1^0 \left(-2\lambda_m^m - 3\lambda_{m+1}^{m+1} |\zeta|^2 + 3\lambda_{m+2}^{m+2} |\zeta|^4 \right) + 12 \left(|\zeta|^2 - \frac{|\zeta|^4}{2} \right) \right] \zeta^m. \quad (6.54)$$

Further, using identity (E 11), we find

$$\delta \mathcal{B}_D^1[\sigma_0] = \left[\frac{|\zeta|^4}{8} - \frac{5|\zeta|^2}{8} + \frac{1}{4} \right] \zeta \quad (6.55)$$

and

$$\delta \mathcal{B}_D^m[\sigma_0] = \left[\frac{|\zeta|^4}{8} - \frac{|\zeta|^2}{4} \left(1 + \frac{1}{m(m+1)} \right) + \frac{1}{4m(m-1)} \right] \zeta^m \quad \text{for } m \geq 2. \quad (6.56)$$

For $m = 1$ this gives $\mathcal{S}[p_1] + \delta \mathcal{S}_D^m[p_0] + (1/16)\delta \mathcal{B}_D^m[\sigma_0] = 0$ so that $\sigma_b^1 = 0$. Using Eq. (6.47), for $m \geq 2$ this yields the $O(\varepsilon)$ interface velocity

$$\begin{aligned} (\tilde{\mathbf{u}}_1 \cdot \hat{\mathbf{r}})(e^{i\theta}) &= -\text{Re} \left[\frac{\partial}{\partial r} \left(\mathcal{S}_D[p_1] + \delta \mathcal{S}_D^m[p_0] + \frac{1}{16} \delta \mathcal{B}_D^m[\sigma_0] \right) \right] \Big|_{\zeta=e^{i\theta}} \\ &= \frac{1}{96} \left[m \frac{\lambda_1^0 \lambda_m^m}{4} - \frac{9}{2(m-1)(2m+1)} \right] \cos m\theta \\ &=: \sigma_b^m \cos m\theta. \end{aligned} \quad (6.57)$$

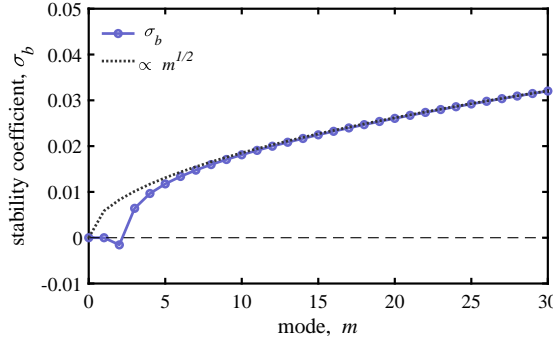


Figure 6. Stability coefficient σ_b^m for buoyancy-dominated flow ($Ra \rightarrow \infty$). For $m = 0, 1$, stability is marginal ($\sigma_b^0 = \sigma_b^1 = 0$), which is reflective of scale and translational invariance, respectively. All other coefficients are positive, indicating buoyancy-driven flows are destabilizing, and tend towards positive infinity as $O(m^{1/2})$.

A plot of σ_b^m is shown in Fig. 6. Both the $m = 0$ and $m = 1$ modes have $\sigma_b^m = 0$, which is consistent with scale and translational invariance. The $m = 2$ mode, which corresponds to an ellipsoidal-like perturbation, is negative, while all other modes are positive with an asymptotic scaling of $\sigma_b^m = O(m^{1/2})$ as in the growth-dominated case. This shows buoyancy-induced flows have a destabilizing effect.

6.5. Stability criterion

Combining the two solutions, the interface evolves as

$$\frac{\partial \mathbf{r}^m}{\partial t} = R \left(\frac{1}{2} + \varepsilon (\sigma_g^m + R^2 \beta Ra \sigma_b^m) \cos m\theta \right) \hat{\mathbf{n}} + O(\varepsilon^2), \quad (6.58)$$

where we emphasize R , ε , and $\hat{\mathbf{n}}$ depend on time. Differentiating the representation (6.1) in time, using $\hat{\mathbf{n}} = \hat{\mathbf{r}} + \varepsilon(m+1) \sin m\theta \hat{\theta} + O(\varepsilon^2)$, and matching powers of ε , one can find a set of differential equations for R and ε . However, the normal and tangential components are incompatible. This can be resolved by adding an arbitrary tangential velocity $\varepsilon T(\theta, t) \sin m\theta \hat{\mathbf{n}}^\perp$ to the interface velocity which does not affect the geometry. Equation (6.58) then becomes

$$\begin{aligned} \frac{\dot{R}}{R} \hat{\mathbf{r}} + \dot{\varepsilon} \left(\cos m\theta \hat{\mathbf{r}} + \sin m\theta \hat{\theta} \right) &= \frac{1}{2} \hat{\mathbf{r}} + \varepsilon \left[\left(-\frac{\dot{R}}{R} + \sigma_g^m + R^2 \beta Ra \sigma_b^m \right) \cos m\theta \hat{\mathbf{r}} \right. \\ &\quad \left. + \left(-\frac{\dot{R}}{R} + \frac{(m+1)}{2} + \frac{T(\theta, t)}{R} \right) \sin m\theta \hat{\theta} \right] + O(\varepsilon^2), \end{aligned} \quad (6.59)$$

from which we see $T(\theta, t) = R \left[-(m+1)/2 + \sigma_g^m + R^2 Ra \sigma_b^m \right]$ ensures compatibility in the $\hat{\mathbf{r}}$ and $\hat{\theta}$ components. Matching powers of ε , we therefore have the coupled ODEs

$$\dot{R} = \frac{R}{2}, \quad (6.60)$$

$$\dot{\varepsilon} = \left(-\frac{\dot{R}}{R} + \sigma_g^m + R^2 \beta Ra \sigma_b^m \right) \varepsilon, \quad (6.61)$$

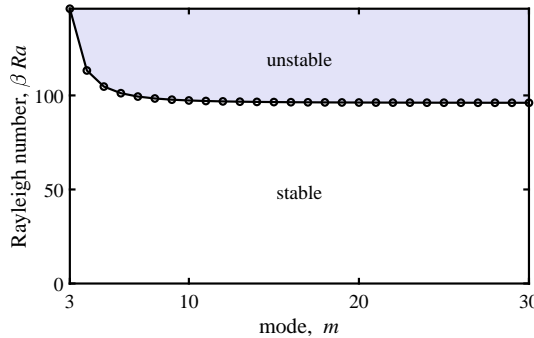


Figure 7. Stable (white) and unstable (purple) regions in the $m - \beta Ra$ plane corresponding to the short time solution (6.64). The black line and circle markers denote the stability threshold βRa_*^m given by Eq. (6.65). This critical value decreases with m , and asymptotically approaches a positive constant $\lim_{m \rightarrow \infty} \beta Ra_*^m = 96$.

with initial conditions $R(0) = 1$ and $\varepsilon(0) = \varepsilon_0 \ll 1$. The $O(1)$ solution always evolves as $R(t) = e^{t/2}$, corresponding to the axisymmetric case. Substituting this into the ε equation, we have

$$\frac{d\varepsilon}{dt} = \left(-\frac{1}{2} + \sigma_g^m + e^t \beta Ra \sigma_b^m \right) \varepsilon. \quad (6.62)$$

The solution to this equation is a combined exponential and double exponential,

$$\varepsilon(t) = \varepsilon_0 e^{(\sigma_g^m - 1/2)t + \beta Ra \sigma_b^m (e^t - 1)}. \quad (6.63)$$

For small t we may expand the upper exponential so that

$$\varepsilon(t) = \varepsilon_0 e^{[(\sigma_g^m - 1/2) + \beta Ra \sigma_b^m]t} + O(t^2). \quad (6.64)$$

Thus, on short time scales, the condition for instability of mode m , for $m > 2$, is

$$Ra > Ra_*^m := \frac{1/2 - \sigma_g^m}{\beta \sigma_b^m} = \frac{96}{\beta} \frac{1}{\left(1 - \frac{18}{(m-1)(2m+1) \lambda_1^0 \lambda_m^m} \right)}. \quad (6.65)$$

A phase diagram depicting this stability threshold is shown in Fig. 7. The critical Rayleigh number decreases with m and asymptotically approaches $\lim_{m \rightarrow \infty} \beta Ra_*^m = 96$. As previously noted, this limit is the threshold for which the axisymmetric pressure is everywhere negative in D . From a physical interpretation, negative pressure acts to compress the droplet but is forbidden to by the divergence constraint. This qualitative change in the pressure, and correspondingly the velocity, can be seen in Fig. 8, where we also see a local maximum in the radial velocity outside the droplet at the transition point.

7. Discussion

We developed and analyzed a model for the growth of a microbial droplet suspended on the surface of a viscous fluid. The integro-differential formulation, which is posed solely on the droplet, naturally leads to axisymmetric solutions and allowed us to rigorously analyze their linear stability. Here we found growth stabilizes the axisymmetric solution at all scales while buoyancy-induced flows are destabilizing, with the smallest scale perturbations growing the fastest.

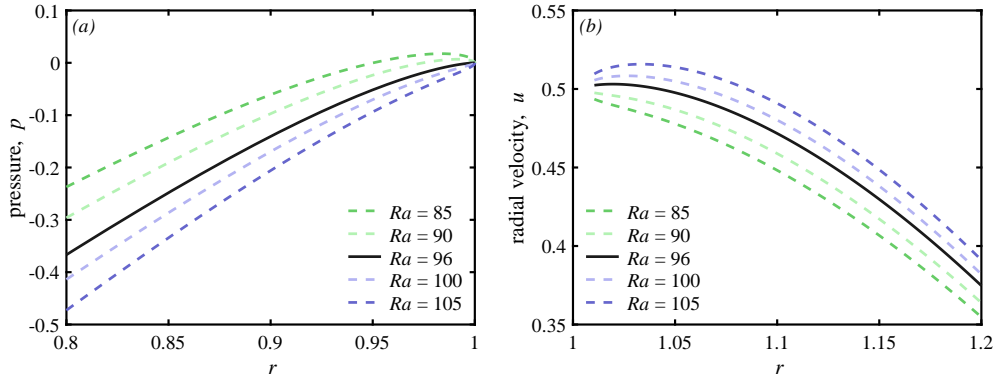


Figure 8. Axisymmetric (a) pressure and (b) velocity near the transition to instability $Ra = 96$ (solid line) for $\beta = 1$. In the former, as Ra crosses the critical value, the pressure becomes negative everywhere and its normal derivative changes sign. In the latter, the normal derivative of the radial velocity changes sign and a local maximum appears outside the droplet.

These results provide an analytical description of the onset of pattern formation observed in yeast colonies growing on viscous substrates (Atis *et al.* 2019). The stability threshold we identified, $\beta Ra = 96$, is the correct order of magnitude for the initial instability observed in experiments, which occurs at a viscosity around $\mu \approx 450 \text{ Pa s}$, or $Ra \approx 50$ as estimated in section 2.4. Moreover, instability of high frequency modes implies the interface will be rough at the smallest scales, which is also consistent with the thin fingers that are observed. The predicted dependence on a single dimensionless parameter can readily be tested in a laboratory setting by varying the substrate viscosity, droplet size, and cell growth rate.

The model and its integro-differential formulation requires the domain to be semi-infinite. In reality, experiments are done on relatively shallow domains. These effects can be captured by tuning the integration constant, but future work may directly compute the solution for finite size domains. This can be done using a similar approach to that taken by Jia *et al.* (2022), where the Fourier transform of the associated Green's function can be found analytically, or by directly using the free-space Green's function of the Boussinesq-Stokes system. Boundedness will introduce recirculating flows owing to fluid incompressibility, and these may have consequences for stability.

For large deformations of the droplet where linear theory breaks down, we must resort to numerical solution. This is a challenging task owing to both solving the free boundary problem, which requires tracking a highly corrugated interface, and evaluating singular integral operators with non-smooth densities (Bruno & Lintner 2013; Helsing & Jiang 2022; Zhou *et al.* 2025). The conformal mapping approach used for the linear stability analysis is a first step in this direction, however adaptive schemes will likely be required when the conformal distortion becomes large.

Another aspect of the experiments in the high metabolic Rayleigh number regime is the breakup of the microbial droplet (Atis *et al.* 2019). The dynamics in this regime can be explored numerically using multi-component methods, which will inherently rely on an accurate resolution of the single droplet problem discussed above, or phase-field models for handling topological changes. When the number of droplets is large, the long-range flows generated by both buoyancy and growth may induce collective behaviors among the disjoint domains, and the effect of this on nutrient transport can be explored.

Acknowledgements We thank Severine Atis and Michael Shelley for useful discussions. The Flatiron Institute is a division of the Simons Foundation.

Data Availability The data that support the findings of this study are openly available at <https://github.com/scottweady/microbial-droplets>.

Declaration of Interests The authors report no conflict of interest.

Appendix A. Numerical validation

In this section we verify our calculations through numerical solution of the $O(1)$ and $O(\varepsilon)$ equations. The numerical methods used here also provide a baseline for solving the integro-differential equation under more general conditions that do not admit exact solutions. This requires a procedure for computing the operators \mathcal{S}_D , \mathcal{N}_D , \mathcal{V}_D , and \mathcal{B}_D . A central challenge is the singular kernel of the operators \mathcal{S}_D and \mathcal{N}_D and, moreover, the finite-part integral in the latter. Here we exploit the spectral properties of these operators to evaluate them numerically.

A.1. Eigenfunction expansions and quadrature

Given a function $v(\mathbf{x})$, we wish to determine the (complex-valued) coefficients \hat{v}_ℓ^m such that

$$v(\mathbf{x}) = \sum_{\ell,m} \hat{v}_\ell^m y_\ell^m(\mathbf{x}), \quad (\text{A } 1)$$

where the sum is taken over even $\ell + m$ when $v \in C^\infty(D)$ and odd $\ell + m$ when $v/\omega \in C^\infty(D)$. In practice, we choose a maximal degree M such that the eigenfunction expansion is truncated at $0 \leq \ell \leq M$ and $|m| \leq \ell$. Using the orthogonality relation for the projected spherical harmonics, we have, for each admissible pair (ℓ, m) ,

$$\hat{v}_\ell^m = \int_D \frac{y_\ell^{m*}(\mathbf{x}) v(\mathbf{x})}{\omega(\mathbf{x})} d\mathbf{x}. \quad (\text{A } 2)$$

To evaluate this integral, we make the change of coordinates $\mathbf{x}(s, \theta) = \sqrt{1-s^2}(\cos \theta, \sin \theta)$ with $(s, \theta) \in [0, 1] \times [0, 2\pi]$, for which the integral becomes

$$\hat{v}_\ell^m = \int_0^1 \int_0^{2\pi} y_\ell^{m*}(s, \theta) v(s, \theta) ds d\theta. \quad (\text{A } 3)$$

This double integral can be evaluated with spectral accuracy using Gauss-Legendre quadrature in s along with the trapezoidal rule in θ . In discrete form, given a function $f(\mathbf{x}) = f(s, \theta)$ on D , this is given by

$$\int_D f(\mathbf{x}) d\mathbf{x} \approx \sum_{i=0}^{N_s-1} \sum_{j=0}^{N_\theta-1} f(s_i, \theta_j) s_i w_i w_j, \quad (\text{A } 4)$$

where s_i and w_i are the Gauss-Legendre nodes and weights of order N_s , and $\theta_j = 2\pi j/N_\theta$ are equispaced points on the interval $[0, 2\pi]$ with corresponding weights $w_j = 2\pi/N_\theta$. Note that the factor s_i cancels when computing the weighted inner product (A 2). The number of quadrature nodes must be high enough to resolve the eigenfunctions. To do so, we choose $N_s = M + 1$ and $N_\theta = 2M + 1$.

A.2. Numerical evaluation of \mathcal{S}_D

Now suppose $v(\mathbf{x}) = \tilde{v}(\mathbf{x})/\omega(\mathbf{x})$ where $\tilde{v} \in C^\infty(D)$ is smooth and $\omega(\mathbf{x}) = \sqrt{1 - |\mathbf{x}|^2}$ as before. We expand \tilde{v} in the even basis of projected spherical harmonics so that

$$v(\mathbf{x}) = \frac{1}{\omega(\mathbf{x})} \left(\sum_{\ell+m \text{ even}} \hat{v}_\ell^m y_\ell^m(\mathbf{x}) \right), \quad (\text{A } 5)$$

where \hat{v}_ℓ^m are approximated by Eqs. (A 3)-(A 4). Applying \mathcal{S}_D , we find

$$\mathcal{S}_D[v](\mathbf{x}) = \frac{1}{4} \left(\sum_{\ell+m \text{ even}} \lambda_\ell^m \hat{v}_\ell^m y_\ell^m(\mathbf{x}) \right). \quad (\text{A } 6)$$

This also provides a straightforward method for solving a system of the form $\mathcal{S}_D[v] = f$ with $f \in C^\infty(D)$. Namely, writing

$$f(\mathbf{x}) = \sum_{\ell+m \text{ even}} \hat{f}_\ell^m y_\ell^m(\mathbf{x}), \quad (\text{A } 7)$$

we have

$$\nu(\mathbf{x}) = \frac{4}{\omega(\mathbf{x})} \left(\sum_{\ell+m \text{ even}} \frac{\hat{f}_\ell^m}{\lambda_\ell^m} y_\ell^m(\mathbf{x}) \right). \quad (\text{A } 8)$$

A.3. Numerical evaluation of \mathcal{N}_D

The procedure for evaluating \mathcal{N}_D is analogous to that for \mathcal{S}_D . Let $\nu(\mathbf{x})$ be such that $\nu(\mathbf{x})/\omega(\mathbf{x}) \in C^\infty(D)$. We expand ν in the odd basis of projected spherical harmonics so that

$$\nu(\mathbf{x}) = \sum_{\ell+m \text{ odd}} \hat{v}_\ell^m y_\ell^m(\mathbf{x}), \quad (\text{A } 9)$$

where \hat{v}_ℓ^m are approximated by Eqs. (A 3)-(A 4). Applying \mathcal{N}_D , we find

$$\mathcal{N}_D[\nu](\mathbf{x}) = -\frac{1}{\omega(\mathbf{x})} \left(\sum_{\ell+m \text{ odd}} \frac{1}{\lambda_\ell^m} \hat{v}_\ell^m y_\ell^m(\mathbf{x}) \right). \quad (\text{A } 10)$$

As before, this provides a straightforward method for solving a system of the form $\mathcal{N}_D[\nu] = f$ with $f \in C^\infty(D)$. Namely, writing

$$f(\mathbf{x}) = \frac{1}{\omega(\mathbf{x})} \left(\sum_{\ell+m \text{ odd}} \hat{f}_\ell^m y_\ell^m(\mathbf{x}) \right), \quad (\text{A } 11)$$

we have

$$\nu(\mathbf{x}) = - \left(\sum_{\ell+m \text{ odd}} \lambda_\ell^m \hat{f}_\ell^m y_\ell^m(\mathbf{x}) \right). \quad (\text{A } 12)$$

A.4. Numerical evaluation of \mathcal{V}_D

We need to compute integrals of the form

$$\mathcal{V}_D[\nu](\mathbf{x}) = \frac{1}{2\pi} \int_D \log |\mathbf{x} - \mathbf{x}'| \nu(\mathbf{x}') \, d\mathbf{x}'. \quad (\text{A } 13)$$

This can be accurately evaluated using singularity subtraction. Specifically, we decompose

$$\begin{aligned} \mathcal{V}_D[\nu](\mathbf{x}) &= -\frac{1}{2\pi} \int_D \log |\mathbf{x} - \mathbf{x}'| (\nu(\mathbf{x}) - \nu(\mathbf{x}')) \, d\mathbf{x}' + \left(\frac{1}{2\pi} \int_D \log |\mathbf{x} - \mathbf{x}'| \, d\mathbf{x}' \right) \nu(\mathbf{x}) \\ &= -\frac{1}{2\pi} \int_D \log |\mathbf{x} - \mathbf{x}'| (\nu(\mathbf{x}) - \nu(\mathbf{x}')) \, d\mathbf{x}' + \left(\frac{|\mathbf{x}|^2 - 1}{4} \right) \nu(\mathbf{x}). \end{aligned} \quad (\text{A } 14)$$

If ν is Hölder continuous on D we have $\lim_{\mathbf{x}' \rightarrow \mathbf{x}} \log |\mathbf{x} - \mathbf{x}'| (\nu(\mathbf{x}) - \nu(\mathbf{x}')) = 0$ and the first integral can be treated with the smooth quadrature rule (A 4).

A.5. Numerical evaluation of \mathcal{B}_D

We need to compute integrals of the form

$$\mathcal{B}_D[\nu](\mathbf{x}) = \frac{1}{8\pi} \int_D |\mathbf{x} - \mathbf{x}'|^2 (\log |\mathbf{x} - \mathbf{x}'| - 1) \nu(\mathbf{x}') \, d\mathbf{x}'. \quad (\text{A } 15)$$

If ν is bounded on D the integrand vanishes for $\mathbf{x} = \mathbf{x}'$ and this integral can be directly evaluated using the quadrature rule (A 4).

Figure 9(a) compares the numerical solution for the stability coefficient to the exact solution for perturbations up to $m = 8$. The convergence study in panel (b) shows the growth stability coefficient σ_g^m is resolved to near machine precision for all M , which is consistent with the fact that the solution is exactly representable in the projected spherical harmonic basis. The buoyancy stability coefficient appears to converge as $O(M^{-4})$, achieving approximately eight digits of accuracy for an expansion of degree $M = 128$.

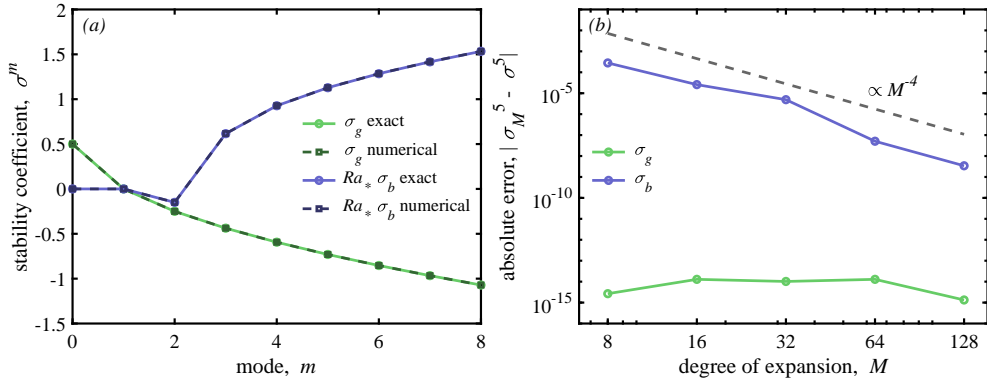


Figure 9. (a) Comparison between the exact and numerical stability coefficients for $M = 32$. The two are essentially indistinguishable across all modes tested. (b) A refinement study shows the numerical solution for the buoyancy coefficient σ_b^m converges at roughly $O(M^{-4})$ order while σ_g^m is resolved to near machine precision.

Appendix B. Derivation of the integral operators

The real-space velocity is given by the inverse Fourier transform of Eqs. (3.6)-(3.7). Defining

$$I_n(\mathbf{x}, z) = \mathcal{F}^{-1}[k^n e^{kz}] (\mathbf{x}, z) \quad (\text{B } 1)$$

and performing a bit of algebra, the three-dimensional velocity $\mathbf{U} = (\mathbf{u}, w)$ can be expressed as

$$\mathbf{u}(\mathbf{x}, z) = -\nabla_{2D} \left[\left(\frac{1}{2} I_{-1} + \frac{z}{2} I_0 \right) * (\chi_{\Omega} p) + \frac{Ra}{16} \left(I_{-4} - z I_{-3} - z^2 I_{-2} \right) * (\chi_{\Omega} \sigma) \right], \quad (\text{B } 2)$$

$$w(\mathbf{x}, z) = - \left[\frac{z}{2} I_1 * (\chi_{\Omega} p) + \frac{Ra}{16} \left(z I_{-2} - z^2 I_{-1} \right) * (\chi_{\Omega} \sigma) \right], \quad (\text{B } 3)$$

where $*$ denotes convolution over \mathbb{R}^2 . We are faced with the difficulty that for $n < -1$ the I_n are not classically integrable and must be interpreted in a distributional sense. However, notice that $\partial_z^j I_n(\mathbf{x}, z) = I_{n+j}(\mathbf{x}, z)$ so that we only need to compute I_{-4} . We interpret this as the solution to the equation $\Delta_{2D}^2(I_{-4}) = \mathcal{F}^{-1}[e^{kz}]$. The right hand side is

$$\begin{aligned} \mathcal{F}^{-1}[e^{kz}] &= \frac{1}{2\pi} \int_0^\infty k e^{kz} J_0(|\mathbf{x}|k) dk \\ &= -\frac{1}{2\pi} \frac{z}{(|\mathbf{x}|^2 + z^2)^{3/2}}, \end{aligned} \quad (\text{B } 4)$$

where J_α is the Bessel function of the first kind. We therefore seek solutions in the variable $r = |\mathbf{x}|$, which yields the general solution

$$\begin{aligned} 8\pi I_{-4}(r, z) &= c_1 r^2 \log r + c_2 r^2 + c_3 \log r + c_4 \\ &+ \left(-3z\sqrt{r^2 + z^2} + (z^2 - r^2) \log \left(\frac{r^2}{\sqrt{r^2 + z^2} - z} \right) - z^2 \log \left(\sqrt{r^2 + z^2} - z \right) \right), \end{aligned} \quad (\text{B } 5)$$

where c_1, c_2, c_3, c_4 are integration constants which may depend on z . In order for this solution to be finite in the limit $r \rightarrow 0$, we must have $c_3 = -2z^2$. Moreover, for continuity in the limit $z \rightarrow 0$ for which I_{-4} is the Green's function of the bilaplacian, we must have $c_1 = 2$. It remains to determine c_2 and c_4 . We can relate these two constants using the condition $(\Delta_{2D} + \partial_z^2) I_{-4} = 0$, which gives $c_4'' = -(r^2 c_2'' + 4c_2 + 4)$. For c_4 to be independent of r , we require $c_2(z) = Az + B$. This shows $c_4(z) = -(2A/3)z^3 - 2(B+1)z^2 + Cz + D$. Because \mathbf{u} is a gradient in \mathbf{x} , it can be shown that the constants A, C, D do not affect the solution and can be set to zero without loss of generality. This leaves the single free constant B . We can simplify I_{-4} to

$$I_{-4}(r, z) = \frac{1}{8\pi} \left((r^2 - z^2) \left(\log \left(\sqrt{r^2 + z^2} - z \right) + B \right) - 3z\sqrt{r^2 + z^2} - 2z^2 \right). \quad (\text{B } 6)$$

V. Gomez Herrera and S. Weady

The expressions for $I_{-3}, I_{-2}, I_{-1}, I_0, I_1$ can be recovered by differentiating this with respect to z , however the full expressions are cumbersome and we omit them here. For $z = 0$ the relevant operators are

$$I_{-4}(r, 0) = \frac{1}{8\pi} r^2 (\log r + B), \quad (\text{B } 7)$$

$$I_{-1}(r, 0) = \frac{1}{2\pi} \frac{1}{r}, \quad (\text{B } 8)$$

from which Eq. (3.23) follows.

Appendix C. Effect of the integration constant

The constant B in the previous section relates to the far-field behavior of the velocity, which non-physically diverges when $Ra > 0$. We interpret the integro-differential equation as an inner solution and B as a matching constant which is chosen such that the vertical velocity vanishes at a domain depth $z = -H$. For analytical convenience, we decompose $B = -\log R - 1 + \kappa$. For $z/r, z/R \gg 1$, we find

$$w(\mathbf{x}, z) = -\frac{Ra}{16} |z| (\log 2|z| + B) \left(\int_{\Omega} \sigma(\mathbf{y}) \, d\mathbf{y} \right) + O(z^{-2}), \quad (\text{C } 1)$$

for which $B = -\log 2|H|$ gives the desired behavior. For the experiments of Atis *et al.* (2019), the dimensionless depth is approximately $|H| \approx 1.4$ (7mm) so that $B \approx -1.03$ and hence $\kappa \approx -0.03$.

Now expanding the operator $\mathcal{B}_{\Omega, \kappa}$ and using the notation $\mathcal{B}_{\Omega} := \mathcal{B}_{\Omega, 0}$, the velocity satisfies

$$\mathbf{u} + \nabla \mathcal{S}_{\Omega}[p] + \frac{Ra}{16} \mathcal{B}_{\Omega}[\sigma] = -\frac{Rak}{16} \nabla \left(\frac{1}{8\pi} \int_{\Omega} |\mathbf{x} - \mathbf{y}|^2 \sigma(\mathbf{y}) \, d\mathbf{y} \right). \quad (\text{C } 2)$$

We write $p = p' + p_{\kappa}$ where p' solves the system with $\kappa = 0$ and p_{κ} satisfies

$$\mathcal{N}_{\Omega}[p_{\kappa}] = -\frac{Rak}{16} \left(\frac{1}{2\pi} \int_{\Omega} \sigma(\mathbf{y}) \, d\mathbf{y} \right). \quad (\text{C } 3)$$

For the nutrient rich case $\gamma(c) = 1$ for which $\sigma = 2\beta$, the right hand side is constant and we see $p_{\kappa} = (R^2\beta Rak/16)p_g$. Following the same stability calculation, this yields

$$\frac{d\epsilon}{dt} = \left[\left(1 + \frac{R^2\beta Rak}{16} \right) \left(-\frac{1}{2} + \sigma_g^m \right) + R^2\beta Ra\sigma_b^m \right] \epsilon. \quad (\text{C } 4)$$

Thus, because $(-1/2 + \sigma_g^m) < 0$ when $m > 0$, larger values of κ have a stabilizing effect. Indeed, for $\kappa \rightarrow -\infty$, which corresponds to $H \rightarrow -\infty$ as described above, all modes are unstable, while for $\kappa \rightarrow +\infty$, which corresponds to $H \rightarrow 0^-$, all modes are stable. Note that the pure growth case $Ra = 0$ is unaffected by the constant.

Appendix D. Recursion relations for the associated Legendre polynomials

Through out this paper we use several non-standard recursion relations of the associated Legendre polynomials. These are

$$P_{\ell+2}^{\ell}(x) = \frac{2\ell+1}{2} \left(-1 + (2\ell+3)x^2 \right) P_{\ell}^{\ell}(x), \quad (\text{D } 1)$$

$$P_{\ell+3}^{\ell}(x) = \frac{2\ell+3}{2} \left(-1 + \left(\frac{2\ell+5}{3} \right) x^2 \right) P_{\ell+1}^{\ell}(x), \quad (\text{D } 2)$$

$$P_{\ell+4}^{\ell}(x) = \frac{(2\ell+1)(2\ell+3)}{8} \left(1 - 2(2\ell+5)x^2 + \frac{1}{3}(2\ell+5)(2\ell+7)x^4 \right) P_{\ell}^{\ell}(x), \quad (\text{D } 3)$$

which also give the convenient identities

$$x^2(1-x^2)^{\ell/2} = \frac{(-1)^{\ell}}{(2\ell+3)!!} \left((2\ell+1)P_{\ell}^{\ell}(x) + 2P_{\ell+2}^{\ell}(x) \right), \quad (\text{D } 4)$$

$$x^3(1-x^2)^{\ell/2} = 3 \frac{(-1)^{\ell}}{(2\ell+5)!!} \left((2\ell+3)P_{\ell+1}^{\ell}(x) + 2P_{\ell+3}^{\ell}(x) \right) \quad (\text{D } 5)$$

$$x^4(1-x^2)^{\ell/2} = 3 \frac{(-1)^{\ell}}{(2\ell+1)!!} \left(8P_{\ell+4}^{\ell}(x) + 4(2\ell+5)P_{\ell+2}^{\ell}(x) + (2\ell+1)(2\ell+7)P_{\ell}^{\ell}(x) \right). \quad (\text{D } 6)$$

Appendix E. Explicit evaluation of volume potentials

In this section we evaluate the volume potentials $\mathcal{B}_D[\zeta'^m]$ and $\mathcal{V}_D[\zeta'^m]$. We will encounter integrals of the form

$$A_{p,q}(z) = \int_D \log |z - \zeta| |\zeta|^p \zeta^q \, d\zeta. \quad (\text{E1})$$

For $z \in \mathbb{C} \setminus D$ and $\zeta \in D$, we can make use of the expansion

$$\log |z - \zeta| = \log |z| - \sum_{k=1}^{\infty} \frac{1}{2k} \left[\left(\frac{\zeta}{z} \right)^k + \left(\frac{\bar{\zeta}}{\bar{z}} \right)^k \right]. \quad (\text{E2})$$

Using this expansion and orthogonality of the Fourier modes, we find

$$A_{p,q}(z) = \begin{cases} -\frac{\pi}{(p+2)|q|} \frac{1}{|z|^q} & q < 0, \\ \frac{2\pi}{(p+2)} \log |z| & q = 0, \\ -\frac{\pi}{(p+2+2q)q} \frac{z^q}{|z|^{2q}} & q > 0, \end{cases} \quad \text{for } z \in \mathbb{C} \setminus D. \quad (\text{E3})$$

E.1. Laplacian

We have $\mathcal{V}_D[\zeta'^m](z) = A_{0,m}(z)/2\pi$ and can apply Eq. (E3) immediately,

$$\mathcal{V}_D[\zeta'^m](z) = \begin{cases} \frac{\log |z|}{2} & m = 0, \\ -\frac{1}{4m(m+1)} \frac{z^m}{|z|^{2m}} & m > 0, \end{cases} \quad \text{for } z \in \mathbb{C} \setminus D. \quad (\text{E4})$$

Noting that $\Delta \mathcal{V}_D[\zeta'^m] = \zeta'^m$ in D , we have the general solution on the interior for all $m \geq 0$,

$$\mathcal{V}_D[\zeta'^m] = (a_m |\zeta|^2 + b_m) \zeta'^m \quad \text{for } \zeta \in D, \quad (\text{E5})$$

where $a_m = 1/(4(m+1))$. The coefficient b_m can be determined by enforcing continuity of the solution across the boundary of D , which gives

$$b_m = \begin{cases} 0 & m = 0, \\ -\frac{1}{4m} & m \geq 1. \end{cases} \quad (\text{E6})$$

E.2. Bilaplacian

Expanding $|z - \zeta|^2 = |z|^2 + |\zeta|^2 - z\bar{\zeta} - \bar{z}\zeta$, we have

$$\mathcal{B}_D[\zeta'^m](z) = \frac{1}{8\pi} \left[|z|^2 A_{0,m} - z A_{2,m-1} - \bar{z} A_{0,m+1} + A_{2,m} - \left(\int_D |z - \zeta'|^2 \zeta'^m d\zeta' \right) \right]. \quad (\text{E7})$$

We treat the $m = 0$ and $m = 1$ terms separately,

$$\mathcal{B}_D[1](z) = \frac{1}{8} \left(|z|^2 \log |z| - |z|^2 + \frac{\log |z|}{2} \right) \quad \text{for } z \in \mathbb{C} \setminus D, \quad (\text{E8})$$

and

$$\mathcal{B}_D[\zeta'](z) = \frac{1}{16} \left(-|z|^2 \log |z| + \frac{|z|^2}{2} - \frac{1}{6} \right) \frac{z}{|z|^2} \quad \text{for } z \in \mathbb{C} \setminus D. \quad (\text{E9})$$

For $m \geq 2$, we get

$$\mathcal{B}_D[\zeta'^m](z) = \frac{1}{16m(m+1)} \left(\frac{|z|^2}{m-1} - \frac{1}{m+2} \right) \frac{z^m}{|z|^{2m}} \quad \text{for } z \in \mathbb{C} \setminus D. \quad (\text{E10})$$

Noting that $\Delta^2 \mathcal{B}_D[\zeta'^m] = \zeta'^m$ in D , we have the general solution on the interior for all $m \geq 0$,

$$\mathcal{B}_D[\zeta'^m] = (a_m |\zeta|^4 + b_m |\zeta|^2 + c_m) \zeta'^m \quad \text{for } \zeta \in D, \quad (\text{E11})$$

where $a_m = 1/(32(m+1)(m+2))$. As before, the coefficients b_m and c_m can be determined by enforcing continuity of the solution and its radial derivative across the boundary of D , which gives

$$b_m = \begin{cases} -\frac{1}{16} & m = 0, \\ -\frac{1}{16m(m+1)} & m \geq 1, \end{cases} \quad (\text{E12})$$

and

$$c_m = \begin{cases} -\frac{5}{64} & m = 0, \\ \frac{3}{64} & m = 1, \\ \frac{1}{32m(m-1)} & m \geq 2. \end{cases} \quad (\text{E 13})$$

Appendix F. Stability of the rigid substrate solution

In this section we perform a linear stability analysis of the rigid substrate problem

$$\mathbf{u} + \nabla p = \mathbf{0} \quad \text{in } \mathcal{Q}_\varepsilon^m, \quad (\text{F 1})$$

$$\nabla \cdot \mathbf{u} = 1 \quad \text{in } \mathcal{Q}_\varepsilon^m, \quad (\text{F 2})$$

$$p = 0 \quad \text{on } \partial \mathcal{Q}_\varepsilon^m, \quad (\text{F 3})$$

where $\mathcal{Q}_\varepsilon^m$ is as in section 6 (see e.g. Weady *et al.* (2024) for further description of this model). Eliminating the velocity, we have

$$-\Delta p = 1 \quad \text{in } \mathcal{Q}_\varepsilon^m, \quad (\text{F 4})$$

$$p = 0 \quad \text{on } \partial \mathcal{Q}_\varepsilon^m. \quad (\text{F 5})$$

Restating these equations on the unit disk in terms of the conformal map $f_{R,\varepsilon}^m$, the pressure satisfies

$$-\tilde{\Delta}(p \circ f_{R,\varepsilon}^m) = J f_{R,\varepsilon}^m \quad \text{in } D, \quad (\text{F 6})$$

$$p \circ f_{R,\varepsilon}^m = 0 \quad \text{on } \partial D. \quad (\text{F 7})$$

Making the expansion $p \circ f_{R,\varepsilon}^m(\zeta) = R^2(p_0(\zeta) + \varepsilon p_1(\zeta))$, we get the $O(1)$ equation

$$-\tilde{\Delta}p_0 = 1 \quad \text{in } D, \quad (\text{F 8})$$

$$p_0 = 0 \quad \text{on } \partial D, \quad (\text{F 9})$$

and the $O(\varepsilon)$ equation

$$-\tilde{\Delta}p_1 = 2(m+1)\zeta^m \quad \text{in } D, \quad (\text{F 10})$$

$$p_1 = 0 \quad \text{on } \partial D. \quad (\text{F 11})$$

It is readily checked that $p_0(\zeta) = (1 - |\zeta|^2)/4$ and $p_1(\zeta) = \zeta^m(1 - |\zeta|^2)/2$ satisfy the equations and boundary conditions. The normal interface velocity is therefore

$$\begin{aligned} (\mathbf{u} \cdot \hat{\mathbf{n}})(\theta) &= \text{Re} [R(\tilde{\mathbf{u}} \cdot \hat{\mathbf{r}})|_{e^{i\theta}}] \\ &= -R \left[\frac{\partial p_0}{\partial r} + \varepsilon \text{Re} \left(-(m+1)\zeta^m \frac{\partial p_0}{\partial r} + \frac{\partial p_1}{\partial r} \right) \Big|_{e^{i\theta}} \right] + O(\varepsilon^2) \\ &= R \left[\frac{1}{2} - \varepsilon \left(\frac{m-1}{2} \right) \cos m\theta \right] + O(\varepsilon^2). \end{aligned} \quad (\text{F 12})$$

Following the same approach as in section 6 with initial data $R(0) = 1$ and $\varepsilon(0) = \varepsilon_0$, we have $R(t) = e^{t/2}$ and $\varepsilon(t) = \varepsilon_0 e^{-mt/2}$. Thus, the axisymmetric solution is stable to all perturbations and the damping rate is linear in m .

REFERENCES

ABRAHAM, EDWARD R 1998 The generation of plankton patchiness by turbulent stirring. *Nature* **391** (6667), 577–580.

ALEXANDER, JAMES C, BERNOFF, ANDREW J, MANN, ELIZABETH K, MANN, J ADIN, WINTERSMITH, JACOB R & ZOU, LU 2007 Domain relaxation in Langmuir films. *Journal of Fluid Mechanics* **571**, 191–219.

ASKHAM, TRAVIS, HOSKINS, JEREMY G, NEKRASOV, PETER & RACHH, MANAS 2025 Integral equations for flexural-gravity waves: analysis and numerical methods. *arXiv preprint arXiv:2501.00887*.

ASP, MERRILL E, HO THANH, MINH-TRI, GERMANN, DANIELLE A, CARROLL, ROBERT J, FRANCESKI, ALANA, WELCH, ROY D, GOPINATH, ARVIND & PATTESON, ALISON E 2022 Spreading rates of bacterial colonies depend on substrate stiffness and permeability. *PNAS nexus* **1** (1), pgac025.

ATIS, SEVERINE, WEINSTEIN, BRYAN T, MURRAY, ANDREW W & NELSON, DAVID R 2019 Microbial range expansions on liquid substrates. *Physical review X* **9** (2), 021058.

AUNG, THINZAR & KIM, MI JEONG 2024 A comprehensive review on kombucha biofilms: A promising candidate for sustainable food product development. *Trends in Food Science & Technology* **144**, 104325.

BENZI, ROBERTO, NELSON, DAVID R, SHANKAR, SURAJ, TOSCHI, FEDERICO & ZHU, XIAOJUE 2022 Spatial population genetics with fluid flow. *Reports on Progress in Physics* **85** (9), 096601.

BOERSMA, J & DANICK, E 1993 On the solution of an integral equation arising in potential problems for circular and elliptic disks. *SIAM Journal on Applied Mathematics* **53** (4), 931–941.

BRUNO, OSCAR P & LINTNER, STÉPHANE K 2013 A high-order integral solver for scalar problems of diffraction by screens and apertures in three-dimensional space. *Journal of Computational Physics* **252**, 250–274.

CHAKRABARTI, A 2000 On the solution of the problem of scattering of surface–water waves by the edge of an ice cover. *Proceedings of the Royal Society of London. Series A: Mathematical, Physical and Engineering Sciences* **456** (1997), 1087–1099.

CHANG, YA-WEN, FRAGKOPoulos, ALEXANDROS A, MARQUEZ, SAMANTHA M, KIM, HAROLD D, ANGELINI, THOMAS E & FERNÁNDEZ-NIEVES, ALBERTO 2015 Biofilm formation in geometries with different surface curvature and oxygen availability. *New Journal of Physics* **17** (3), 033017.

COSTABEL, MARTIN, DAUGE, MONIQUE & DUDUCHAVA, ROLAND 2003 Asymptotics without logarithmic terms for crack problems. *Communications in Partial Differential Equations* **28**, 869–926.

FAIZA, NUZHAT, WELCH, ROY & PATTESON, ALISON 2025 Substrate stiffness modulates collective colony expansion of the social bacterium *Myxococcus xanthus*. *APL bioengineering* **9** (1).

FEI, CHENYI, MAO, SHENG, YAN, JING, ALERT, RICARD, STONE, HOWARD A, BASSLER, BONNIE L, WINGREEN, NED S & KOŠMRLJ, ANDREJ 2020 Nonuniform growth and surface friction determine bacterial biofilm morphology on soft substrates. *Proceedings of the National Academy of Sciences* **117** (14), 7622–7632.

FEI, WENJIE, GU, YANG & BISHOP, KYLE JM 2017 Active colloidal particles at fluid–fluid interfaces. *Current opinion in colloid & interface science* **32**, 57–68.

GONZALEZ LA CORTE, SEBASTIAN, STEVENS, COREY A, CÁRCAMO-OYARCE, GERARDO, RIBBECK, KATHARINA, WINGREEN, NED S & DATTA, SUJIT S 2025 Morphogenesis of bacterial cables in polymeric environments. *Science Advances* **11** (3), eadq7797.

GREENSPAN, HARVEY P 1976 On the growth and stability of cell cultures and solid tumors. *Journal of theoretical biology* **56** (1), 229–242.

GU, HUAN, CHEN, AARON, SONG, XINRAN, BRASCH, MEGAN E, HENDERSON, JAMES H & REN, DACHENG 2016 How *Escherichia coli* lands and forms cell clusters on a surface: a new role of surface topography. *Scientific reports* **6** (1), 29516.

HALLATSCHKEK, OSKAR, DATTA, SUJIT S, DRESCHER, KNUT, DUNKEL, JÖRN, ELGETI, JENS, WACLAWS, BARTEK & WINGREEN, NED S 2023 Proliferating active matter. *Nature Reviews Physics* **5** (7), 407–419.

HALLEGRAEFF, GUSTAAF M 2003 Harmful algal blooms: a global overview. *Manual on harmful marine microalgae* **33**, 1–22.

HELSING, JOHAN & JIANG, SHIDONG 2022 Solving Fredholm second-kind integral equations with singular right-hand sides on non-smooth boundaries. *Journal of Computational Physics* **448**, 110714.

HICKL, VINCENT & JUAREZ, GABRIEL 2022 Tubulation and dispersion of oil by bacterial growth on droplets. *Soft Matter* **18** (37), 7217–7228.

JIA, LEROY L, IRVINE, WILLIAM TM & SHELLEY, MICHAEL J 2022 Incompressible active phases at an interface. part 1. formulation and axisymmetric odd flows. *Journal of Fluid Mechanics* **951**, A36.

JIA, LEROY L & SHELLEY, MICHAEL J 2022 The role of monolayer viscosity in Langmuir film hole closure dynamics. *Journal of Fluid Mechanics* **948**, A1.

LOWENGRUB, JOHN S, FRIEBOES, HERMANN B, JIN, FANG, CHUANG, YAO-LI, LI, XIANGRONG, MACKLIN, PAUL, WISE, STEVEN M & CRISTINI, VITTORIO 2009 Nonlinear modelling of cancer: bridging the gap between cells and tumours. *Nonlinearity* **23** (1), R1.

LUBENSKY, DAVID K & GOLDSTEIN, RAYMOND E 1996 Hydrodynamics of monolayer domains at the air–water interface. *Physics of fluids* **8** (4), 843–854.

MANIKANTAN, HARISHANKAR & SQUIRES, TODD M 2020 Surfactant dynamics: hidden variables controlling fluid flows. *Journal of fluid mechanics* **892**, P1.

MARTIN, PA 1996 Mapping flat cracks onto penny-shaped cracks, with application to somewhat circular tensile cracks. *Quarterly of Applied Mathematics* **54** (4), 663–675.

MASOUD, HASSAN & SHELLEY, MICHAEL J 2014 Collective surfing of chemically active particles. *Physical review letters* **112** (12), 128304.

NARAYANASAMY, NISHANT, BINGHAM, EMMA, FADERO, TANNER, BOZDAG, G OZAN, RATCLIFF, WILLIAM C, YUNKER, PETER & THUTUPALLI, SHASHI 2025 Metabolically driven flows enable exponential growth in macroscopic multicellular yeast. *Science Advances* **11** (25), eadr6399.

PEARCE, PHILIP, SONG, BOYA, SKINNER, DOMINIC J, MOK, RACHEL, HARTMANN, RAIMO, SINGH, PRAVEEN K,

JECKEL, HANNAH, OISHI, JEFFREY S, DRESCHER, KNUT & DUNKEL, JÖRN 2019 Flow-induced symmetry breaking in growing bacterial biofilms. *Physical review letters* **123** (25), 258101.

PERLEKAR, P, BENZI, R, NELSON, DR & TOSCHI, F 2010 Population dynamics at high Reynolds number. *Physical Review Letters* **105** (14), 144501–144501.

POSTEK, WITOLD, STAŚKIEWICZ, KLAUDIA, LILJA, ELIN & WAC LAW, BART LOMIEJ 2024 Substrate geometry affects population dynamics in a bacterial biofilm. *Proceedings of the National Academy of Sciences* **121** (17), e2315361121.

PRASAD, M, OBANA, N, LIN, S-Z, ZHAO, S, SAKAI, K, BLANCH-MERCADER, C, PROST, J, NOMURA, N, RUPPRECHT, J-F, FATTACCIOLI, J & OTHERS 2023 *Alcanivorax borkumensis* biofilms enhance oil degradation by interfacial tubulation. *Science* **381** (6659), 748–753.

SAFFMAN, PG 1976 Brownian motion in thin sheets of viscous fluid. *Journal of Fluid Mechanics* **73** (4), 593–602.

SAFFMAN, PG & DELBRÜCK, M 1975 Brownian motion in biological membranes. *Proceedings of the National Academy of Sciences* **72** (8), 3111–3113.

STEPHAN, ERNST P 1987 Boundary integral equations for screen problems in \mathbb{R}^3 . *Integral Equations and Operator Theory* **10** (2), 236–257.

STONE, HA & McCONNELL, HM 1995 Hydrodynamics of quantized shape transitions of lipid domains. *Proceedings of the Royal Society of London. Series A: Mathematical and Physical Sciences* **448** (1932), 97–111.

STONE, HOWARD A & AJDARI, ARMAND 1998 Hydrodynamics of particles embedded in a flat surfactant layer overlying a subphase of finite depth. *Journal of Fluid Mechanics* **369**, 151–173.

STONE, HOWARD A & LEAL, L GARY 1990 The effects of surfactants on drop deformation and breakup. *Journal of Fluid Mechanics* **220**, 161–186.

VACCARI, LIANA, ALLAN, DANIEL B, SHARIFI-MOOD, NIMA, SINGH, AAYUSH R, LEHENY, ROBERT L & STEBE, KATHLEEN J 2015 Films of bacteria at interfaces: three stages of behaviour. *Soft Matter* **11** (30), 6062–6074.

VACCARI, LIANA, MOLAEI, MEHDI, NIEPA, TAGBO HR, LEE, DAEYEON, LEHENY, ROBERT L & STEBE, KATHLEEN J 2017 Films of bacteria at interfaces. *Advances in colloid and interface science* **247**, 561–572.

WEADY, SCOTT, PALMER, BRYCE, LAMSON, ADAM, KIM, TAEYOON, FARHADIFAR, REZA & SHELLEY, MICHAEL J 2024 Mechanics and morphology of proliferating cell collectives with self-inhibiting growth. *Physical Review Letters* **133** (15), 158402.

WILLIAMS, TIMOTHY D & SQUIRE, VERNON A 2004 Oblique scattering of plane flexural-gravity waves by heterogeneities in sea-ice. *Proceedings of the Royal Society of London. Series A: Mathematical, Physical and Engineering Sciences* **460** (2052), 3469–3497.

WOLFE, PETER 1971 Eigenfunctions of the integral equation for the potential of the charged disk. *Journal of Mathematical Physics* **12** (7), 1215–1218.

ZHOU, HAN, YOUNG, YUAN-NAN & MORI, YOICHIRO 2025 Energy variational modeling and numerical simulation of open membranes in Stokes flow. *arXiv preprint arXiv:2504.16823* .